Exploring Tornadic Debris Signature Hypotheses Using Radar Simulations and Large-Eddy Simulations

RACHAEL N. CROSS,[a,b] DAVID J. BODINE,[a,b] ROBERT D. PALMER,[a,b] CASEY GRIFFIN,[c] BOONLENG CHEONG,[b] SEBASTIAN TORRES,[a,d,e] CALEB FULTON,[b,f] JAVIER LUJAN,[b] AND TAKASHI MARUYAMA[g]

[a] *School of Meteorology, University of Oklahoma, Norman, Oklahoma*
[b] *Advanced Radar Research Center, Norman, Oklahoma*
[c] *State University of New York at Brockport, Brockport, New York*
[d] *NOAA/OAR/National Severe Storms Laboratory, Norman, Oklahoma*
[e] *Cooperative Institute for Severe and High-Impact Weather Research, Norman, Oklahoma*
[f] *School of Electrical and Computer Engineering, University of Oklahoma, Norman, Oklahoma*
[g] *Disaster Prevention Research Institute, Kyoto University, Kyoto, Japan*

(Manuscript received 8 December 2022, in final form 22 June 2023, accepted 24 July 2023)

ABSTRACT: When a tornado lofts debris to the height of the radar beam, a signature known as the tornadic debris signature (TDS) can sometimes be observed on radar. The TDS is a useful signature for operational forecasters because it can confirm the presence of a tornado and provide information about the amount of damage occurring. Since real-time estimates of tornadic intensity do not have a high degree of accuracy, past studies have hypothesized that the TDS could also be an indicator of the strength of a tornado. However, few studies have related the tornadic wind field to TDS characteristics because of the difficulty of obtaining accurate, three-dimensional wind data in tornadoes from radar data. With this in mind, the goals of this study are twofold: 1) to investigate the relationships between polarimetric characteristics of TDSs and the three-dimensional tornadic winds, and 2) to define relationships between polarimetric radar variables and debris characteristics. Simulations are performed using a dual-polarization radar simulator called SimRadar; large-eddy simulations (LESs) of tornadoes; and a single-volume, T-matrix-based emulator. Results show that for all simulated debris types increases in horizontal and vertical wind speeds are related to decreases in correlation coefficient and increases in TDS area and height and that, conversely, decreases in horizontal and vertical wind speeds are related to increases in correlation coefficient and decreases in TDS area and height. However, the range of correlation coefficient values varies with debris type, indicating that TDSs that are composed of similar debris types can appear remarkably different on radar in comparison with a TDS with diverse scatterers. Such findings confirm past observational hypotheses and can aid operational forecasters in tornado detection and potentially the categorization of damage severity using radar data.

KEYWORDS: Tornadoes; Radars/radar observations; Large-eddy simulations

1. Introduction

The introduction of dual-polarization capabilities to weather radar has helped distinguish between meteorological and nonmeteorological scatterers, in addition to hydrometeor size, shape, and concentration (Zrnić and Ryzhkov 1999; Straka et al. 2000). Dual-polarization radars are also capable of detecting polarimetric signatures in supercells, such as differential reflectivity (Z_{DR}) arcs, Z_{DR} columns, and the tornadic debris signature (TDS), among others (Ryzhkov et al. 2005b; Kumjian and Ryzhkov 2008; Snyder et al. 2013; Kumjian et al. 2014). The TDS is attributed to lofted debris in tornadoes, allowing the TDS to be used for tornado detection (Ryzhkov et al. 2005b). Ryzhkov et al. (2005b) defined the TDS as a region with correlation coefficient (ρ_{hv}) < 0.8, $Z_{DR} < 0.5$ dB, and a local maximum in radar reflectivity (Z_H; >45 dBZ) that is collocated with a tornadic vortex signature. Bluestein et al. (2007) conducted the first mobile radar study of TDSs where they found that ρ_{hv} is a better indicator of debris than Z_{DR}. However, there are still challenges with detecting weaker tornadoes, as they loft less debris and thus may not produce an observable TDS (Kumjian and Ryzhkov 2008; Van Den Broeke and Jauernic 2014). With this in mind, the threshold of Z_H for a TDS as stated in Ryzhkov et al. (2005b) was modified by Van Den Broeke and Jauernic (2014) and Griffin et al. (2019). In both studies, a lower Z_H threshold (<20 dBZ) was suggested to account for lower concentrations of debris (Van Den Broeke and Jauernic 2014; Griffin et al. 2019).

Operational forecasters have used TDSs to improve tornado detection (Van Den Broeke 2017) and characterize tornado damage. It has been hypothesized that spatial TDS parameters (e.g., TDS height and width) are correlated with tornado damage severity (Schultz et al. 2012; Bodine et al. 2013; Van Den Broeke and Jauernic 2014; Kurdzo et al. 2015; Van Den Broeke 2015, 2017). Likewise, statistics such as 10th percentile ρ_{hv} have been shown to decrease as tornado damage severity increases (Bodine et al. 2013; Griffin et al. 2019). However, determining relationships between the TDS and changes in polarimetric variables for tornado dissipation is more complicated due to debris fallout (Bodine et al. 2013; Houser et al. 2016; McKeown et al. 2020).

While observational studies can make inferences about the lofted debris type, size, and concentration, it is impossible to know exact details of each debris characteristic. Thus, results about debris type, size, and concentration have been largely

Corresponding author: Rachael N. Cross, rey@ou.edu

DOI: 10.1175/JTECH-D-22-0141.1

© 2023 American Meteorological Society. This published article is licensed under the terms of the default AMS reuse license. For information regarding reuse of this content and general copyright information, consult the AMS Copyright Policy (www.ametsoc.org/PUBSReuseLicenses).

Brought to you by NOAA Central Library | Unauthenticated | Downloaded 01/23/24 09:18 PM UTC

TABLE 1. A list of TDS hypotheses from observational studies, and the relevant, supporting literature.

TDS hypotheses	Supporting studies
As debris size increases, ρ_{hv} will decrease	Ryzhkov et al. (2005a) and Bodine et al. (2013, 2016b)
As debris size increases, Z_H will increase	Ryzhkov et al. (2005a) and Bodine et al. (2013, 2016b)
As debris concentration increases, ρ_{hv} will decrease	Wakimoto et al. (2018)
As debris concentration increases, Z_H will increase	Bodine et al. (2013), Dowell et al. (2005), and Wurman and Gill (2000)
As a tornado intensifies, ρ_{hv} will decrease	Bodine et al. (2013) and Griffin et al. (2019)
As a tornado intensifies, Z_H will increase	Dowell et al. (2005)
As a tornado intensifies, the TDS area will increase	Schultz et al. (2012), Bodine et al. (2013), Van Den Broeke and Jauernic (2014), Kurdzo et al. (2015), and Van Den Broeke (2015, 2017)
As a tornado intensifies, the TDS height will increase	Schultz et al. (2012), Bodine et al. (2013), Van Den Broeke and Jauernic (2014), Kurdzo et al. (2015), and Van Den Broeke (2015, 2017)

speculative. For example, it has been hypothesized that, as debris size increases, ρ_{hv} will decrease and Z_H will increase (Bodine et al. 2013, 2016b; Ryzhkov et al. 2005b). Specifically, Bodine et al. (2013) thought that increases in 90th percentile Z_H for violent tornadoes could be due to the lofting of larger debris or higher concentrations of debris. Furthermore, it has been hypothesized that lower ρ_{hv} corresponds to higher debris loading and an increase in the radar-measured tornadic wind speeds (Wakimoto et al. 2018). To summarize, a list of some of these hypotheses is given in Table 1.

The structure of the TDS also varies depending on the intensity of the tornado and the lofted debris types. A commonly seen feature is the weak echo hole (WEH; Wurman and Gill 2000; Dowell et al. 2005) that, on radar, appears as a ring of higher Z_H that encircles a local minimum of Z_H and maximum of ρ_{hv} (Bodine et al. 2014). The local maximum in ρ_{hv} in the WEH is thought to result from a reduction of scatterers that is due to strong vertical motions and the centrifuging of debris (Tanamachi et al. 2012). In a vertical sense, Wakimoto et al. (2015) found a "debris overhang," which is a hook of low ρ_{hv} values arching over a column of high ρ_{hv}. Wakimoto et al. (2015) hypothesized that the column of high ρ_{hv} was collocated with the storm-scale updraft, causing smaller, lighter debris to be lofted into the debris overhang.

Understanding how the TDS structure and parameters evolve throughout the life cycle of a tornado can provide forecasters with information beyond just tornado detection. In an operational warning environment, forecasters use parameters, such as rotational velocity and TDS height, to distinguish between strong/violent (EF2+ on the enhanced Fujita scale) and weak (EF0–1) tornadoes (Gibbs 2016). However, since it is nearly impossible to get vertical velocity data from single-Doppler analyses, most TDS studies have not directly correlated TDS characteristics with updraft speed. Additionally, only qualitative information is currently obtained from observational data about debris types or concentrations. Previous work has been limited to relating general TDS parameters, such as TDS height and width, to EF ratings from damage surveys or horizontal wind components sampled by mobile radars. However, there are large errors in the EF-scale estimates of peak, tornadic wind speeds (Wurman et al. 2021), which further limits efforts to relate TDS parameters to tornadic intensity.

With these observational limitations in mind, this study takes a simulation approach to examine the relationship among debris characteristics, tornadic wind speeds, and polarimetric radar variables. Using large-eddy simulations (LESs) and a dual-polarization radar simulator (SimRadar; Cheong et al. 2017), the evolution of the TDS is examined across a simulated tornado life cycle using physically based models. While several TDS hypotheses have been proposed (Table 1), many of these hypotheses are largely speculative because of incomplete information about debris or tornadic wind speeds. Using simulations allows for the direct comparison of tornado-scale wind speeds with debris type and concentration to systematically test these hypotheses and examine operational applications. Such relationships will provide operational meteorologists with near-real-time information about the evolution of tornado intensity. Researchers also seek to understand the three-dimensional characteristics of debris in tornadoes, as it is pertinent to debris loading and correcting debris centrifuging errors.

Section 2 of this paper outlines the details of the simulations and debris types used in this study. Section 3 describes the results of the simulations while section 4 provides a more detailed discussion of key results. Section 5 provides a summary of the findings from this work. This paper has been adapted from Cross (2021), with the addition of a cumulative debris simulation that is detailed in section 3c.

2. Data and methods

To test hypotheses from past observational studies, this project takes a simulation approach to determining relationships among debris characteristics, the tornadic wind field, and polarimetric weather radar variables. Two different radar emulators are used: a single-volume emulator to relate debris size, type, and concentration to polarimetric weather radar variables and a more complex radar simulator, SimRadar, that can be used to examine the relationship between a tornado-like wind field from large-eddy simulations to polarimetric statistics of an evolving TDS. Both radar emulators and LESs are described in more detail in the following subsections.

a. Single-volume emulator

Values of Z_H, ρ_{hv}, and Z_{DR} were calculated for various debris types, concentrations, and sizes using the equations from Bukovčić et al. (2017). To emulate polarimetric weather radar variables as seen by an S-band radar, a wavelength of 0.1 m

Brought to you by NOAA Central Library | Unauthenticated | Downloaded 01/23/24 09:18 PM UTC

TABLE 2. Details of the scatterer types used in the single-volume-emulator simulations.

Scatterer type	Complex index of refraction	Axis ratio	Equivalent diameter (mm)
Wood boards	1.416 + 0.0706*i*	0.25, 0.33, 0.50	20–300
Rocks	3.000 + 0.0300*i*	0.50, 0.75, 0.90	2–100
Rain	8.990 + 1.4700*i*	0.85	3

was selected with a volume size of 10^6 m^3. A 0.1-m wavelength was chosen to provide comparable results to what is observed by the operational NEXRADs. Scattering amplitudes were obtained using T-matrix calculations (Mishchenko et al. 1996; Mishchenko 2000) for rocks and wood boards. Details about the range of debris diameters, axis ratios, and complex dielectric constants for each debris type are given in Table 2. The dielectric constants for wood boards and rocks are taken from Ulaby et al. (1988) and Senior et al. (1987), respectively.

The T-matrix scattering amplitude calculations approximate each scatterer as a spheroid. The simplified shapes of debris could produce higher values of ρ_{hv} than those seen in observations, as asymmetries in scatterers' shapes can reduce ρ_{hv} (Balakrishnan and Zrnić 1990). However, the T-matrix method still produces reasonable results for comparing changes in polarimetric variables across size and concentration for a given debris type and shape. The T-matrix method also allows for more efficient calculations of the scattering amplitude. For example, calculating the scattering amplitude for a single piece of debris using the more accurate High Frequency Structure Simulator (HFSS) can take a day to complete while the T-matrix method can calculate scattering amplitudes for a range of sizes within a matter of minutes. Thus, the T-matrix method was chosen for portions of the study where the focus was determining relationships between polarimetric radar variables, debris size, and concentration.

The use of multiple axis ratios increased the diversity of scatterer shapes in the resolution volume. The wood board axis ratios created an object with a longer horizontal axis while the rock axis ratios produced a semispherical object. In calculating the polarimetric weather radar variables, the volume was populated with an equal number of randomly oriented debris for each axis ratio. The resultant scattering amplitudes were then averaged across axis ratios before calculating the polarimetric weather radar variables. The averaged scattering amplitudes also produced a more realistic result for ρ_{hv} given that no two debris pieces are exactly the same shape.

Axis ratios of raindrops were calculated using the methodology presented in Thurai and Bringi (2005), which calculates an axis ratio for each drop radius. To produce a uniform field of rain, one drop size for rain was selected by comparing the Z_H values of rain with that of debris. The selected drop size and concentration should result in a relatively similar signal power for rain and debris, such that one scatterer type will not completely dominate the signal. A rain background of 3-mm drops produced Z_H values comparable to debris (49 dBZ for rain and an average of 54 dBZ for debris) and was thus the chosen drop size for the emulator. Meanwhile, the diameter of each debris type was chosen to represent a realistic range of scatterers that could be lofted by a vortex. The range of diameters for wood boards attempts to emulate small 2 in. × 4 in. (5 cm × 10 cm) wood boards, ranging from wood board fragments to small boards with an equivalent diameter of 300 mm (approximately 1 ft). As for rocks, the selected sizes attempt to represent small rocks and gravel.

There were two types of experiments run with the single-volume emulator: one with just debris and one with a combination of rain and debris. In both experiments, the chosen concentrations of debris ranged from 10 to 10^4 m^{-3}. The rain background consisted of 10^8 drops within the volume, leading to a concentration of 10^2 drops per meter cubed.

Last, 1296 orientations were calculated for each debris type and size. These different orientations are created by rotating spheroids from the $+z$ axis and then from the $+y$ axis. The angles of rotation are varied in 5° increments to capture angle-dependent scattering effects. When calculating the polarimetric variables with the single-volume emulator, values of Z_H, ρ_{hv}, and Z_{DR} were averaged across 100 permutations of the same experiment. Since there are a finite number of orientations to choose from, the scattering amplitudes were multiplied by some factor of 10 to obtain concentrations higher than 1000.

b. *SimRadar*

SimRadar is a dual-polarization radar simulator that combines LES model data, 6-degree-of-freedom model (6DOF) debris trajectories, and electromagnetic scattering data. The 6DOF trajectory calculations provide realistic orientations and debris motion required to make calculations of polarimetric variables. Specific details about the 6DOF debris trajectory calculations and the SimRadar platform can be found in Cheong et al. (2017) and Umeyama et al. (2018).

The combination of debris trajectories and the LES model data provides a straightforward method of relating the dynamic, tornado-scale wind and embedded debris field to the evolution of polarimetric radar variables. Unlike with the single-volume emulator, the radar cross sections of debris were calculated using HFSS data that capture electromagnetic effects from more complex shapes (Lujan 2016). For this study, cross sections were calculated for a S-band radar with a simulated radar wavelength of 0.1 m. Three debris types were used in the SimRadar simulations: 2 in. × 4 in. wood boards, leaves, and metal sheets. Details about each debris type can be found in Table 3 and in Lujan (2016).

The radar is located 2100 m from the center of the vortex, and the resolution of each range gate is 75 m. The horizontal domain is wider in the x direction at farther ranges. The average size of the domain is 827 m × 595 m in the x and y directions. In each simulation, SimRadar has a beamwidth of 1° and a pulse repetition time of 0.5 ms. A full list of the radar parameters used are given in Table 4. Because of memory limitations within SimRadar, the highest possible height SimRadar can scan is 718 m. As such, the radar scanned in

Brought to you by NOAA Central Library | Unauthenticated | Downloaded 01/23/24 09:18 PM UTC

TABLE 3. List of scatterer type, dimensions, and density for each debris type used for the SimRadar simulations.

Debris parameters	
Scatterer type	Leaf
Dimensions (body)	1 mm × 80 mm × 60 mm
Dimensions (stem)	120 mm long
Density	350 kg m^{-3}
Mass (body)	0.0017 kg
Complex index of refraction	34.6 + 12.3*i*
Scatterer type	Wood board
Dimensions	50 mm × 300 mm × 100 mm
Density	500 kg m^{-3}
Mass	0.75 kg
Complex index of refraction	2.31 + 0.572*i*
Scatterer type	Metal sheet
Dimensions	1 mm × 1000 mm × 1000 mm
Density	7850 kg m^{-3}
Mass	7.9 kg
Complex index of refraction	1.00 + 0.00*i*

TABLE 4. SimRadar parameters used for every simulation in this study.

Radar parameters	
PRT	0.5 ms
Wavelength	0.1 m
Peak transmit power	50 kW
Transmit pulse width	0.2 μs
Antenna gain	50 dB*i*
Antenna beamwidth	1.0°
Range resolution	75 m
Gate spacing	15 m
Samples per dwell	100
Azimuthal sampling	0.5°
Max unambiguous velocity	50 m s^{-1}

0.5° elevation angle increments from 2.5° (89 m) to 9.0° (318 m). Since 9.0° corresponds to a low height relative to observations, another elevation angle (17.5°; 611 m) was added to represent a higher beam altitude that is more common for NEXRAD radars.

The single-volume simulations were initialized with 101 376 pieces of debris and 2 045 952 raindrops. There are three of these simulations in total: one with leaves, one with wood boards, and one with metal sheets. Raindrops are randomly populated in the SimRadar domain at the onset of a simulation, while debris are initialized at the bottom of the domain. However, not all debris are lofted above 89 m AGL. To illustrate this, the debris count with height is plotted at the end of the tornadogenesis case (Fig. 1). Regardless of debris type, only a fraction of debris are lofted to the lowest height of the radar beam. Specifically, only 19.74% of leaves, 5.52% of wood boards, and 14.69% of metal sheets are lofted past 89 m (2.5° elevation). These percentages correspond to 21.9 leaves, 6.14 wood boards, and 16.3 metal sheets per resolution volume on average. Thus, while 101 376 pieces of debris are initialized in the model, the actual concentration of debris in the vortex is much lower because only a fraction of the initialized debris are lofted.

Two cumulative simulations were run to better represent a realistic TDS that could be seen in observations. These two simulations consisted of equal amounts of leaves, wood boards, and metal sheets. To analyze the effects of concentration on the results, one simulation was run with approximately 10^4 of each debris type (55 296 debris total) and another one with 10^5 of each debris type (304 128 debris total). Because these simulations represent the most realistic case, SimRadar was set to scan in 0.5° elevation angle increments from 2.5° (89 m) to 17.5° (611 m).

1) TDS AREA CALCULATION

The TDS was defined by $\rho_{hv} < 0.95$ for range gates within 200-m radius from the vortex center. This radial threshold is 1.5–2 times the time-averaged radius of maximum wind. These criteria were used for all objective debris discrimination. No Z_H threshold was used as Z_H was generally high throughout the domain. The center of the tornado was manually chosen by selecting the region where the simulated radial velocities were near zero within the couplet. To calculate the TDS area, the number of gates meeting the aforementioned requirements were recorded and then multiplied by the area of each gate.

The 0.95 threshold for ρ_{hv} was motivated by the intrinsically high values of ρ_{hv} for the leaf debris type. The leaves had ρ_{hv} values that always exceeded the 0.8 threshold used in Ryzhkov et al. (2005b) and rarely dropped below 0.9. These high ρ_{hv} values have been seen in past work with observational TDS cases, where it is speculated that ρ_{hv} is higher in areas of light debris, such as leaves (e.g., Griffin et al. 2019). While not every debris type used in this study is "light," the same 0.95 threshold was used for all simulations for ease of comparison across debris types. However, increasing the ρ_{hv} threshold reduces the effectiveness of discriminating between meteorological and nonmeteorological scatterers (i.e., rain and debris).

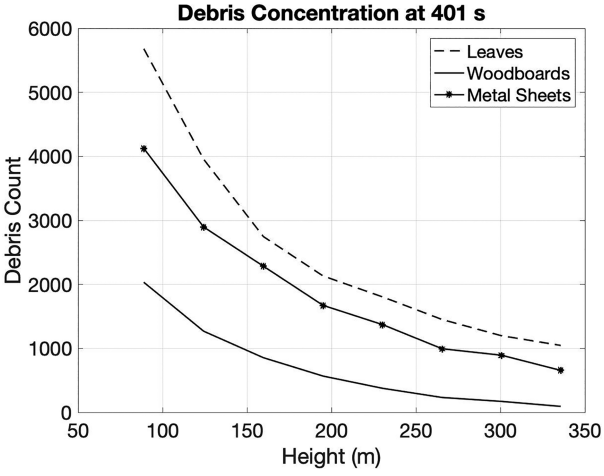

FIG. 1. The number of leaves (dashed line), wood boards (solid line), and metal sheets (connected scatter points) at each elevation at the end of the tornadogenesis simulation.

Brought to you by NOAA Central Library | Unauthenticated | Downloaded 01/23/24 09:18 PM UTC

With this in mind, calculations of TDS area were also performed with the same 0.8 threshold suggested in Ryzhkov et al. (2005a) for comparison.

The sensitivity of the results to the chosen radial threshold was also tested by calculating the TDS area using $r < 300$ m and no radial threshold. For each tested threshold, the overall trends in TDS area for each debris type were similar. The only difference was an increase in size of the TDS area, which is to be expected for larger radial thresholds.

2) TDS HEIGHT CALCULATIONS

Calculations of the TDS height were done for each debris type. The TDS height for a given time was defined as the maximum height at which a TDS was detected and a TDS was present at all elevation angles below it. The TDS was detected as long as one grid point satisfied the TDS criteria (grid points with $\rho_{hv} < 0.95$ within $r < 200$ m). The rate of change of the TDS height was also calculated by subtracting the minimum peak TDS height from the maximum peak TDS height, and the resulting difference was divided by the time over which this change occurred.

c. *Large-eddy simulations*

To simulate a tornado-like vortex, the LES was modified using the methods outlined in Maruyama (2011) and Bodine et al. (2016a). The setup for the simulation consisted of a spinup period to allow for it to reach steady state. After reaching a steady state, the full life cycle of a tornado was simulated by changing the boundary conditions for each phase: genesis, vortex breakdown, and dissipation. This study only focuses on the genesis and dissipation phases as they are the most relevant to the TDS hypotheses proposed by past work (Table 1). Furthermore, each phase is treated as its own, distinct simulation with time restarting from $t_0 = 0$ s at the onset of each phase.

Each simulation produces a vortex with similar outer boundary conditions (e.g., an inflow layer, an updraft, and in some cases, a central downdraft); however, in all cases friction is accounted for by imposing a surface roughness length (Z_0) of 0.1 m. Each simulation is defined by a shallow inflow layer where the horizontal boundary conditions (BCs) impose an approximately axisymmetric flow through the inflow region. In the tornadogenesis simulation, this inflow region starts with a depth of approximately 500 m and ends with a depth between 200 and 300 m. In the dissipation simulation, this inflow region ends with a depth of approximately 500 m and starts with a depth between 200 and 300 m. The selected inflow depth represents the mesocyclone-scale flow, and changes of this depth increase the domainwide swirl ratio, analogous to tornado vortex chamber experiments (e.g., Church et al. 1979). Additionally, the corner flow develops as a response to the preset BCs and is shallower than the mesocyclone-scale inflow. Although the depth of the corner flow (not shown) varies throughout each simulation, it is relatively close to the range (10–20 m) suggested by Wurman et al. (2013) and Kosiba and Wurman (2013). Each stage of the LES model simulations has a unique set of initial BCs imposed on the top of the domain, all of which are given in Table 5. The BCs are linearly interpolated in time between simulation start times.

TABLE 5. Boundary condition values for updraft speed and angular momentum for each phase of the LES. Note that the vortex breakdown and dissipation start correspond to the end of previous simulation stage. The length of each phase is also given. Only the tornadogenesis and dissipation cases were used in this study.

LES simulation	Updraft speed (m s^{-1})	Angular momentum (m^2 s^{-1})	Length of simulation (s)
Tornadogenesis start	15	2000	408.16
Vortex breakdown start	25	13 500	408.16
Dissipation start	20	30 000	816.33
Dissipation end	15	2000	

The LES model employs a stretched grid with finer grid spacing that increases from 2.6 to 16.8 m out from the center of the vortex and from 2.7 to 98 m from the surface of the domain. The full domain of each LES model is 2 km × 2 km × 1.5 km in the x, y, and z directions. As previously mentioned, to increase the computational efficiency of the SimRadar simulations, a subset of the total domain is used. The dimensions of this subset are 977 m × 977 m × 718 m.

1) TORNADOGENESIS CASE

The tornadogenesis simulation is the first phase of an LES model run that simulates the entire life cycle of a vortex. The genesis phase lasts for 408.16 s, after which the vortex breakdown case begins and the single-cell tornado transitions to a two-cell vortex. At the beginning of the genesis simulation, the vortex meanders about the origin of the domain as the tornado intensifies (Figs. 2a,b). By the end of the simulation, the tornado has widened and is a one-cell vortex oriented at the center of the domain (Fig. 2c). At the end of the genesis case, a very narrow (<100 m wide), axial downdraft descends to the bottom of the tornado. This descending downdraft marks the end of the genesis phase and the beginning of vortex breakdown.

The maximum updraft begins at 24 m s^{-1} and intensifies to 101 m s^{-1} while the maximum 2D wind magnitude begins at 37 m s^{-1} and increases to 135 m s^{-1}, which represents an EF5 tornado. The development of 99th-percentile horizontal velocity (hereby called $V_{H,99}$), 99th-percentile vertical velocity (hereby called W_{99}), and 99th-percentile vertical vorticity (hereby called ζ_{99}) are given in Fig. 3a, reaching maximum values at the end of the simulation.

2) TORNADO DISSIPATION CASE

Since the full model run was split into three phases—vortex genesis, breakdown, and dissipation—the dissipation simulation begins at $t_0 = 0$ s. The dissipation phase begins with an intense, two-cell vortex with a central downdraft (Fig. 2d). At this time, there are two pockets of stronger vertical velocities oriented to the west and east of the central downdraft. As the

Brought to you by NOAA Central Library | Unauthenticated | Downloaded 01/23/24 09:18 PM UTC

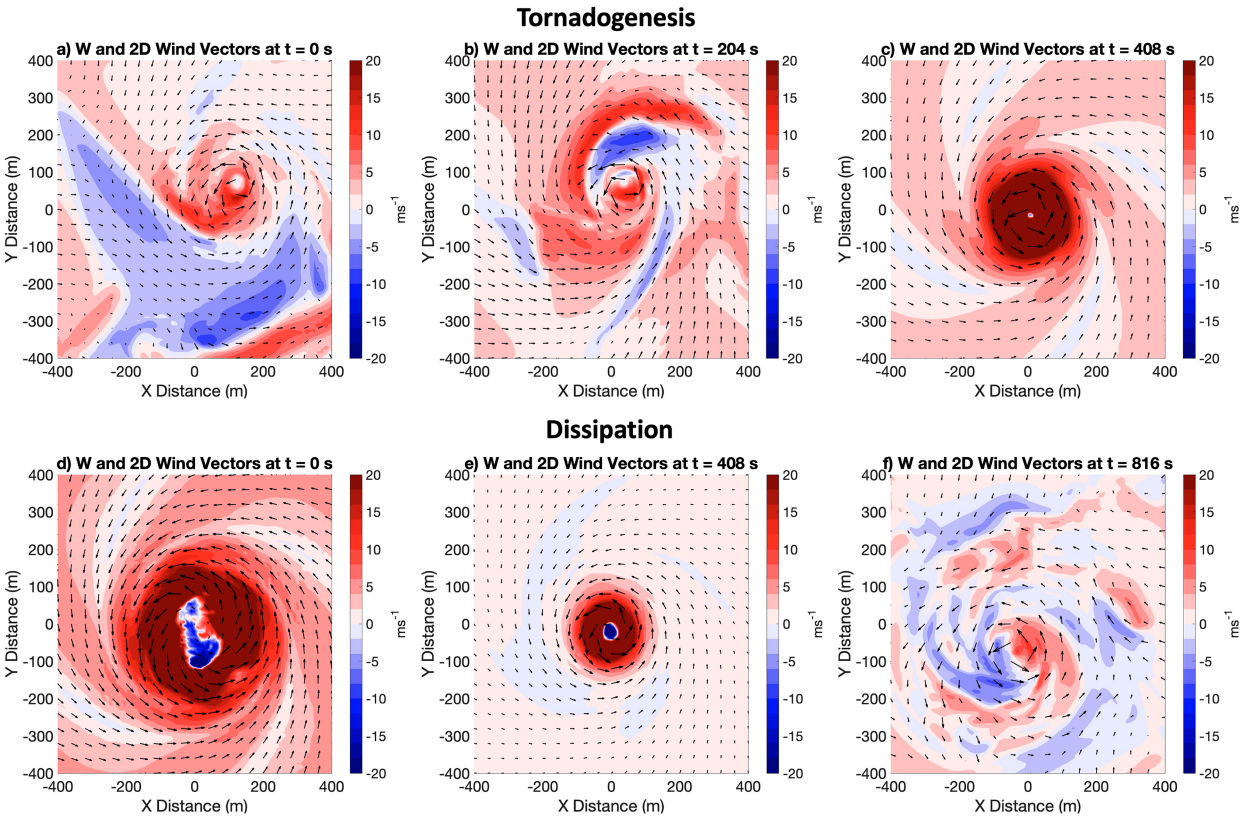

FIG. 2. Horizontal cross sections of vertical velocity (color fill) and 2D wind vectors (arrows) for the (a)–(c) tornadogenesis and (d)–(f) dissipation simulation at 83 m AGL. The top and bottom panels each correspond to separate simulations starting from $t_0 = 0$ s.

simulation progresses, the vortex weakens and narrows (Fig. 2e). The center of the tornado remains near the origin of the domain until the end of the simulation when it cycles about the origin of the domain as the tornado weakens (Fig. 2f). The length of this simulation is 816.32 s, which is 2 times the length of the tornadogenesis simulations, and the evolution of the wind field in this simulation is given in Fig. 3b. In this case, the tornado takes longer to dissipate than it did to form in the genesis phase, which is consistent with the slower tornado decay seen in radar-based observations of these processes (French et al. 2014; Houser et al. 2015; Griffin et al. 2019). The maximum updraft begins at 87 m s^{-1} and weakens to 24 m s^{-1} while the maximum 2D wind magnitude starts at 52 m s^{-1} and ends at 9 m s^{-1}. The rate of change of the BCs during the first half of the simulation is the same as the rate of change of the BCs for the tornadogenesis simulations. During the second half of the dissipation simulation, the BCs remain constant and are the same as the initial conditions as the tornadogenesis simulations.

3. Results

a. *Single-volume emulator: Debris characteristics versus polarimetric variables*

To determine how different debris characteristics change polarimetric weather radar variables, the single-volume emulator was used to calculate values of Z_H and ρ_{hv} for wood boards and rocks. These polarimetric weather radar variables were calculated for different debris sizes and concentrations. Values of Z_{DR} were also calculated but are not shown as 1) no discernible trends were noted for Z_{DR} across debris size and concentration and 2) the list of hypotheses in Table 1 focuses on trends in ρ_{hv} and Z_H.

In general, ρ_{hv} decreases as debris size increases for both wood boards and rocks (Figs. 4a,c). This decrease is neither monotonic nor linear and occurs most notably between wood board sizes of 100–225 mm, with a slight increase in ρ_{hv} for $D > 225$ mm. For rocks, ρ_{hv} generally decreases between diameters of 25–100 mm. A comparison of both debris types shows that wood boards with $D < 100$ mm have $\rho_{hv} > 0.95$ whereas rocks with $D < 100$ mm have ρ_{hv} between 0.4 and 1.

To better understand why ρ_{hv} is lower for rocks at small debris sizes, two test simulations were run: 1) wood boards with an axis ratio of 0.5 and diameters from 2 to 100 mm and 2) rocks with the same axis ratio and diameter range. The only difference between these two simulations was the dielectric constant. The resulting range of ρ_{hv} (not shown) was approximately 0.1–0.95 for rocks and 0.95–1 for wood boards. Thus, the dielectric constant can largely impact ρ_{hv}, meaning that under the conditions in these simulations, it takes larger wood boards to lower ρ_{hv} relative to rocks.

When increasing the concentration of debris in the debris-only experiments, ρ_{hv} values remain constant for both rocks and wood boards (Figs. 4a,c). With the addition of a uniform

Brought to you by NOAA Central Library | Unauthenticated | Downloaded 01/23/24 09:18 PM UTC

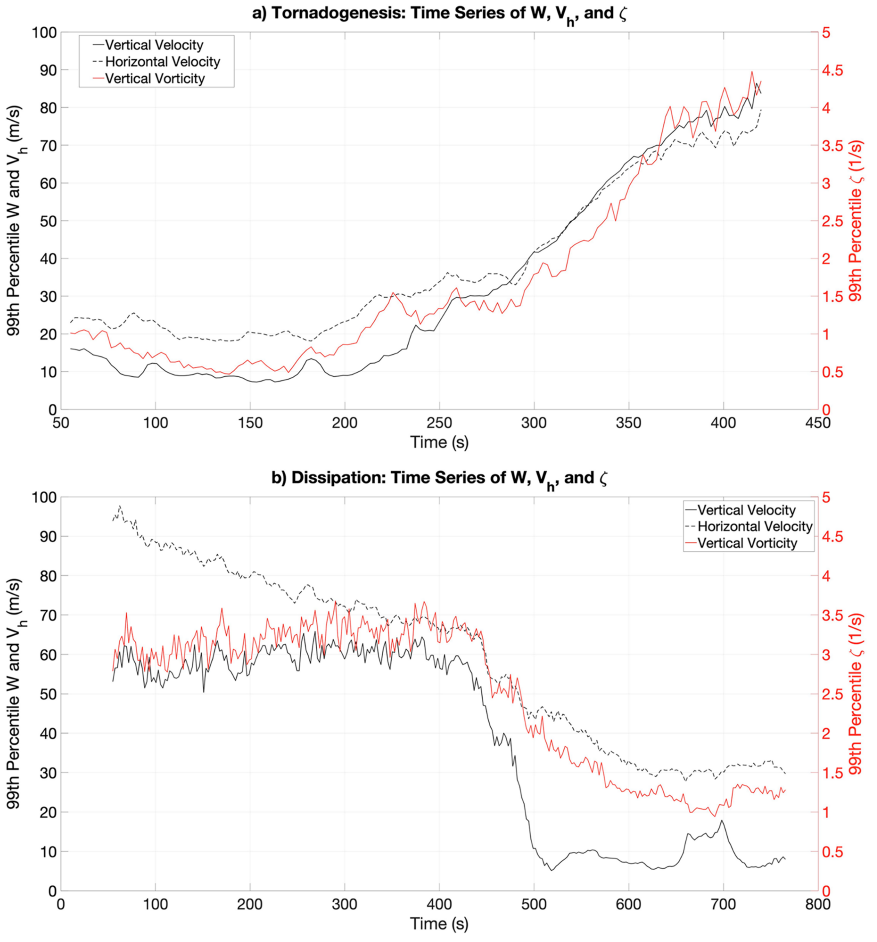

FIG. 3. Evolution of W_{99}, $V_{H,99}$, and ζ_{99} for (a) the tornadogenesis simulation at 83 m from 0 to 408 s and (b) the dissipation simulation at 83 m from 0 to 816 s. The top and bottom panels each correspond to separate simulations starting from $t = 0$ s.

rain background, however, ρ_{hv} begins to decrease with increasing debris concentration (Figs. 4b,d). The amount of decrease is not consistent, with ρ_{hv} decreasing the most between concentrations of 10 and 100 for wood boards and rocks. For both debris types, the trend at the highest concentration matches the trend in the debris-only experiments, indicating debris dominates the backscattered signal at these concentrations. Thus, ρ_{hv} decreases as debris become the more dominant scatterer type.

Meanwhile, Z_H generally increases with increasing debris size for both rocks and wood boards (Figs. 5a,c). The sharp increase in Z_H seen across the smallest rock diameters is likely due to these sizes (<20 mm) falling in the Rayleigh scattering regime, where Z_H is related to the scatterer diameter to the sixth power. For $D > 20$ mm, Z_H increases less drastically due to resonance effects. This transition in scattering regimes explains why the range of Z_H is larger for rocks than it is for wood boards, despite the wood boards having a wider array of sizes. Last, for the higher-concentration experiments (1000 and 10 000), values of dBZ exceed those commonly seen in observations (70–80 dBZ).

Values of Z_H generally show a linear relationship with debris concentration as there is a consistent increase of Z_H with increasing debris concentration (Figs. 5a,c). This linear increase of Z_H is unsurprising given the equation for Z_H is directly proportional to the number concentration of scatterers. When adding rain, the baseline Z_H is increased (Figs. 5b,d), meaning for low debris concentrations, the resulting Z_H value is that of the rain background. In this case, it is only for cases in which debris dominates the signal that Z_H increases with increasing debris concentration.

b. *Simulated relationships among tornadic wind speeds, debris, and TDSs*

While the single-volume emulator allows for the calculation of polarimetric radar variables across multiple debris types, sizes, and concentrations, it cannot relate polarimetric data to the evolving tornadic wind speeds. To test hypotheses regarding TDS characteristics and the tornadic wind field, a more realistic radar simulator (SimRadar) was used with LESs of a tornado-like vortex. The results of these simulations are detailed in the following subsections.

Brought to you by NOAA Central Library | Unauthenticated | Downloaded 01/23/24 09:18 PM UTC

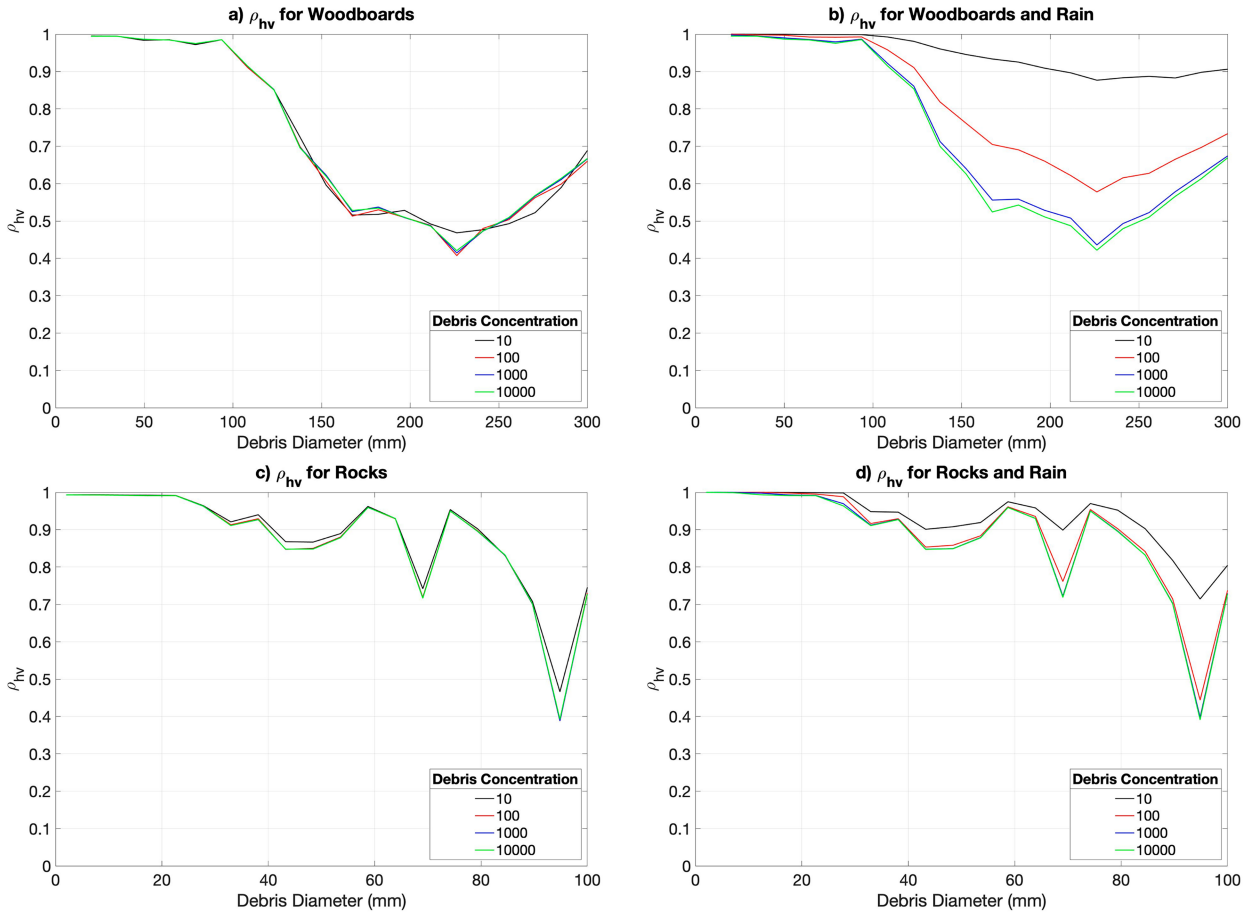

FIG. 4. Plot of ρ_{hv} for (a) wood boards, (b) rain and wood boards, (c) rocks, and (d) rain and rocks for different debris sizes. Each individual value corresponds to a concentration of 100 debris items at that specific debris size. Values of ρ_{hv} are calculated using the single-volume emulator.

1) TORNADOGENESIS CASE

To evaluate how ρ_{hv} and Z_H evolve during tornadogenesis, 10th-percentile ρ_{hv} (hereby called ρ_{10}), 90th-percentile Z_H (hereby called Z_{90}), $V_{H,99}$, and W_{99} were calculated at elevation angles of 2.5° and 5.0°. Values of ρ_{10} and Z_{90} were calculated in two ways: 1) from the distribution of ρ_{hv} and Z_H in the entire PPI and 2) from points only within the TDS. While results from both methods are discussed, only ρ_{10} and Z_{90} from the first method are shown in Fig. 6 for brevity.

Values of ρ_{10} and Z_{90} calculated from the entire PPI are discussed first. For the leaves, ρ_{10} remained relatively high during the first 200 s since little to no debris was lofted (Fig. 6a). The tornado began to intensify at 200 s, as is evident from the gradual increase in W_{99} and $V_{H,99}$. At this time, ρ_{10} for leaves decreased, first at the 2.5° elevation angle followed by a smaller decrease at 5.0°. While all three debris types experienced some reduction in ρ_{10} as the vortex intensified (Figs. 6a,c,e), the range of ρ_{10} differs for each debris type. For leaves, ρ_{10} drops to near 0.9; for wood boards, ρ_{10} drops to 0.2; and for metal sheets, ρ_{10} decreases to values between 0.6 and 0.8 depending on the height of the measurement. Wood boards exhibit the lowest values of ρ_{10} despite having the lowest concentration (Fig. 1), meaning the magnitude of the drop in ρ_{10} is likely more a function of debris type than concentration.

Values of ρ_{10} from within the TDS exhibit similar trends as seen in Fig. 6 (not shown). Because of the 0.95 ρ_{hv} threshold used to define the TDS, values of ρ_{10} within the TDS begin at lower values relative to those in Fig. 6. Both the wood boards and metal sheet TDSs experience decreasing ρ_{10} over time; however, the leaf TDS has relatively constant values of ρ_{10} throughout the simulation. The constant ρ_{10} in the leaf TDS is likely due to the leaves having intrinsically higher ρ_{hv} than the other debris types. Given these differences between ρ_{10} within the TDS and ρ_{10} for the entire PPI, values of ρ_{10} are sensitive to the chosen ρ_{hv} and radial thresholds. However, the general trends seen in ρ_{10} for the PPI and for the TDS are similar.

At 5.0°, ρ_{10} for wood boards decreases sharply at 300 s while ρ_{10} for the other two debris types exhibits a more gradual change (Figs. 6a,c,e). The decrease in ρ_{10} for wood boards at 5.0° occurs when W_{99} is between 30 and 35 m s^{-1} as compared with between 10 and 15 m s^{-1} for leaves and metal sheets. The gradual decrease of ρ_{10} for leaves and metal sheets

Brought to you by NOAA Central Library | Unauthenticated | Downloaded 01/23/24 09:18 PM UTC

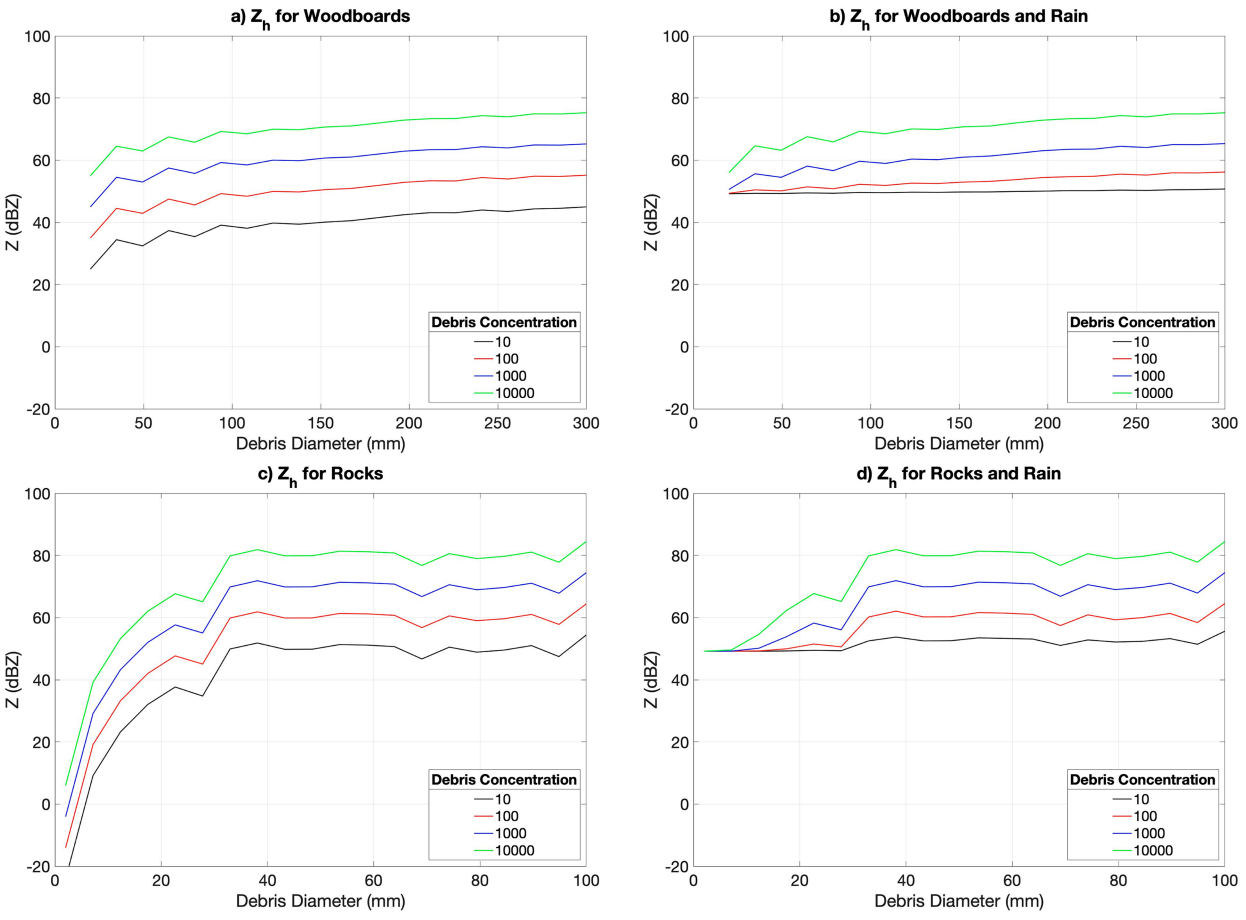

FIG. 5. As in Fig. 4, but Z_H.

indicates a transition of the dominant scatterer type from rain to debris as more debris are lofted by the strengthening updraft. However, the sharp decrease in ρ_{10} for the wood boards has multiple implications. First, results in section 3a show that ρ_{hv} decreases for larger debris and for a signal more dominated by debris (Fig. 4). As the largest debris type (Table 3), a lower concentration of wood boards could reduce ρ_{10} more than the same concentration of smaller debris. Second, the sharp decrease in ρ_{10} when W_{99} reaches 30–35 m s^{-1} could indicate some minimum W_{99} required to loft wood boards. However, this explanation is the least likely as wood boards are not the heaviest debris type (Table 3).

There is also a delay in the decrease of ρ_{10} with height for all debris types. The offset in decreasing ρ_{10} is an indication of the time it takes for debris to be lofted higher up into the vortex. For each debris type, values of ρ_{10} at 2.5° decrease near 200 s, which corresponds to W_{99} values between 5 and 10 m s^{-1} and $V_{H,99}$ values between 20 and 25 m s^{-1}. Wood boards have the most notable delay in decreasing ρ_{10} at 5.0° (Fig. 6c). For wood boards, ρ_{10} decreases near 300 s at 5.0°, which is 100 s later than the time of decrease at 2.5°. In addition, W_{99} increases by approximately 30 m s^{-1} and $V_{H,99}$ increases by 10–15 m s^{-1} during this 100-s delay. For leaves and metal sheets (Figs. 6a,e), ρ_{10} at 5.0° decreases near 225–250 s, which is only a 25–50-s delay. During this 25–50-s period, W_{99} increases by 5 m s^{-1} and $V_{H,99}$ increases by 5–10 m s^{-1}. These results indicate that it takes stronger winds for wood boards to be lofted to 5.0° relative to metal sheets and leaves.

Minimum values of ρ_{hv} were also calculated at the 17.5° level (not shown). The leaf and wood board debris types showed no change in ρ, while ρ_{10} for the metal sheets decreased slightly after 300 s. The consistent nature of ρ_{10} at 611 m in comparison with the more notable changes in ρ_{10} at 89 m indicates that operational radars (such as a NEXRAD) will not always observe trends of ρ_{hv} within the TDS. The lack of a TDS at higher elevations might also be a limitation of SimRadar modeling higher altitudes without a parent storm.

Values of Z_{90} for wood boards, metal sheets, and leaves generally increase with increases in W_{99} and $V_{H,99}$ (Figs. 6b,d,f). However, the magnitude of this increase over time is small, with Z_{90} only increasing by approximately 5 dB at both 2.5° and 5.0°. The same result is seen for Z_{90} within the TDS, though Z_{90} at 5.0° increases by as much as 10 dB throughout the simulation. Since the change in Z_{90} is similar across debris types, changes in ρ_{10} over time are a much better discriminator of debris type than Z_{90}. Looking back to Figs. 4b and 4d, Z_H changed most

Brought to you by NOAA Central Library | Unauthenticated | Downloaded 01/23/24 09:18 PM UTC

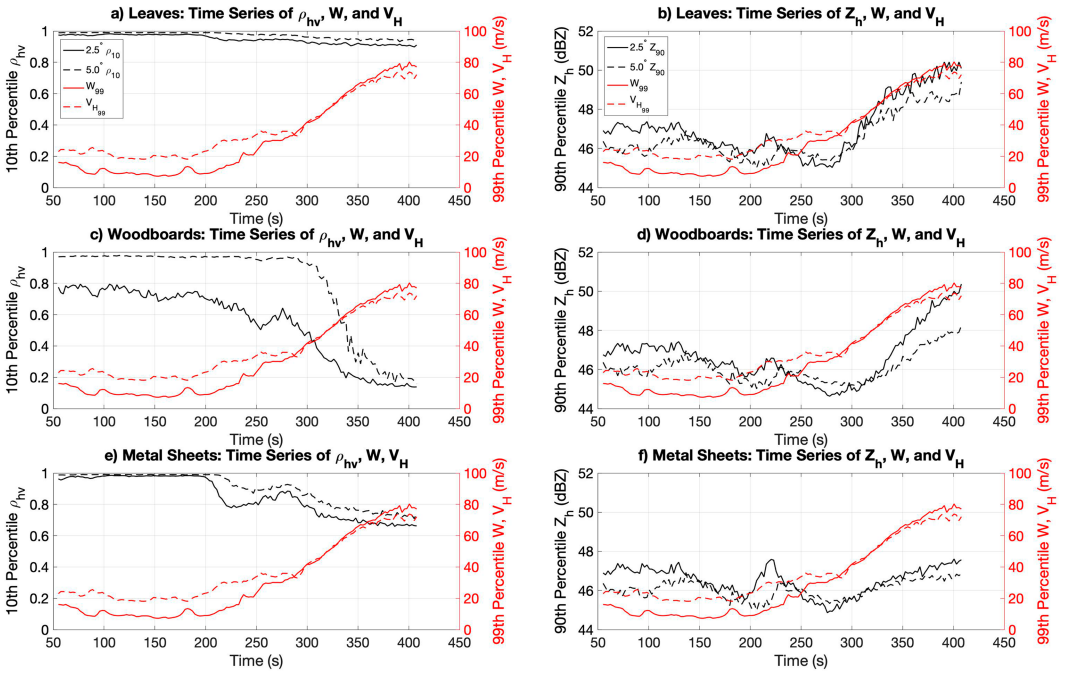

FIG. 6. Time series plots of (left) ρ_{10} and (right) Z_{90} for (a),(b) leaves; (c),(d) wood boards; and (e),(f) metal sheets at 2.5° (solid black line) and 5.0° (dashed black line). On each graph, W_{99} (red line) and $V_{H,99}$ (red dashed line) at 2.5° are also plotted. All values shown are for the entire PPI and are from the tornadogenesis simulation.

drastically for very small debris. Thus, Z_{90} might be a good discriminator between the smallest and largest debris types, especially in the Rayleigh regime, but is not as useful for discriminating across debris with similar size. However, the contribution of rain to Z_H in this simulation could be masking any drastic changes in Z_H.

In addition to values of ρ_{10} and Z_{90}, the area of the TDS was also evaluated throughout the intensification of the vortex (Figs. 7a–c). For each debris type, the area of the TDS increases as W_{99} and $V_{H,99}$ intensifies. The area of the wood board and metal sheet TDS is larger than the area of leaf TDS, which could partially be due to the ρ_{hv} threshold imposed on the calculation of the TDS area. Since ρ_{hv} values within the leaf TDS are very high, there could be resolution volumes with leaves that exceeded the 0.95 ρ_{hv} threshold.

The rate of change of the TDS area throughout the entire simulation is 26 $m^2\ s^{-1}$ for the leaf TDS, 63 $m^2\ s^{-1}$ for the wood board TDS, and 94 $m^2\ s^{-1}$ for the metal sheet TDS. The metal sheet TDS in Fig. 7c increases rapidly in response to small changes in W_{99} and $V_{H,99}$, which could indicate a certain W_{99} and $V_{H,99}$ threshold that, if exceeded, metal sheets are lofted. However, between 250 and 300 s, the TDS area of metal sheets decreases despite increasing W_{99} and $V_{H,99}$. Thus, it is challenging to define a certain W_{99} and $V_{H,99}$ threshold for the lofting of debris, as other factors such as updraft width could also play a role in lofting more scatterers.

In Ryzhkov et al. (2005b), a lower ρ_{hv} threshold of 0.8 is used to define the TDS. To compare the 0.95 ρ_{hv} threshold used in this study with the 0.8 ρ_{hv} threshold defined in Ryzhkov et al. (2005b), the TDS area calculations were rerun using the 0.8 ρ_{hv} and the 200-m radial thresholds. With the Ryzhkov et al. (2005b) ρ_{hv} threshold, the TDS area for wood boards and metal sheets increases slightly later than the 0.95 ρ_{hv} TDS area (Figs. 7b,c). Additionally, there is no discernible TDS for the leaves (Fig. 7a). The lack of a TDS emphasizes that certain debris types do not have ρ_{hv} values that meet the Ryzhkov et al. (2005b) criteria. However, other debris types (metal sheets and wood boards) do have discernible TDSs that widen as the vertical and horizontal winds intensify (Figs. 7b,c). These results highlight that there is no perfect ρ_{hv} threshold for debris, as different debris have intrinsically different ρ_{hv} values.

The spatial structure of the TDS can also provide information about tornado dynamics and changes in intensity. Looking at plan position indicator (PPI) plots of 24-s averages in ρ_{hv} at the end of the tornadogenesis simulation, there are multiple differences in the TDS structure at lower elevations. Looking at the leaf TDS (Fig. 8a), there is a lobe of lower ρ_{hv} values to the northwest and southeast of the vortex center. One thing to note is that the maximum updraft contours are between the lobes of low ρ_{hv} and the center of the tornado. Both of these lobes of low ρ_{hv} are mostly situated within the 10 m s^{-1} updraft contour. Overall, values of ρ_{hv} within the TDS are higher than 0.9, which is consistent with what was seen in Fig. 6a.

The wood board TDS (Fig. 8c) has lower values of ρ_{hv} than the leaf TDS, with ρ_{hv} dropping as low as 0.2. While the leaf TDS splits off into two distinct lobes, the wood board TDS creates a ring of low ρ_{hv} values around a center of higher ρ_{hv}. While at first it may appear that this ring of low ρ_{hv} is

Brought to you by NOAA Central Library | Unauthenticated | Downloaded 01/23/24 09:18 PM UTC

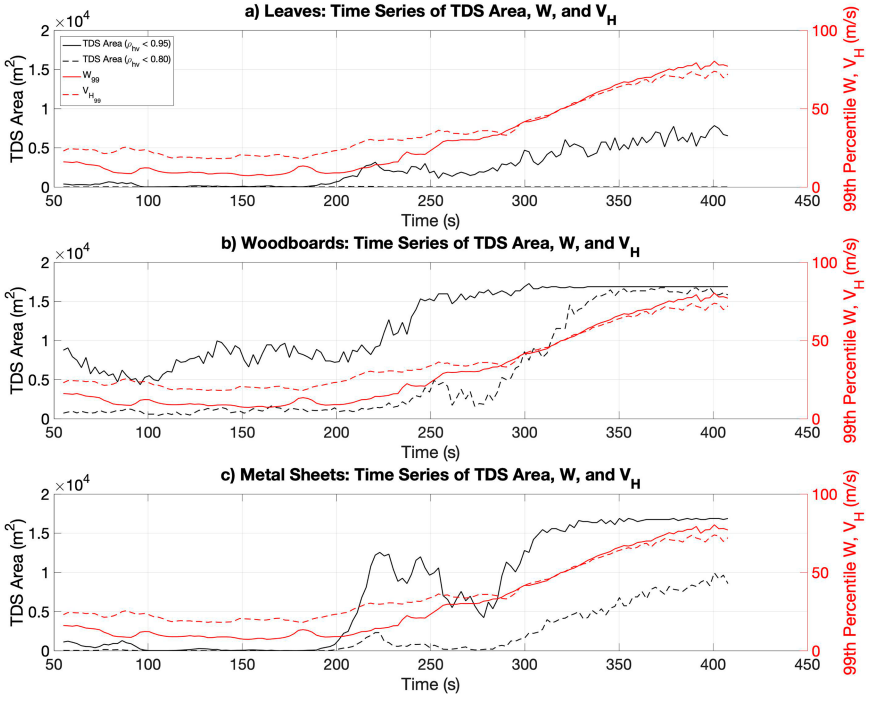

FIG. 7. Time series plots of TDS area for $\rho_{hv} < 0.95$ (black line), TDS area for $\rho_{hv} < 0.8$ (dashed black line), W_{99} (solid red line), and $V_{H,99}$ (dashed red line) for (a) leaves, (b) wood boards, and (c) metal sheets at 89 m AGL for the tornadogenesis simulation.

centrifuged debris, the concentration of debris at 401 s (Fig. 8d) suggests otherwise. For the wood boards, the highest concentration of debris is collocated with the local ρ_{hv} maxima near the maximum updraft. This pattern is also somewhat seen with the leaves when comparing Figs. 8a and 8b. The highest concentration of leaves, while more spread out than the wood boards, is located approximately in the middle of the two lobes of lower ρ_{hv}. One hypothesis why this occurs in these simulations is the fact there is only one debris type and size present. The reduced diversity of scatterers leads to higher values of ρ_{hv}. Thus, the regions of lower ρ_{hv} in Figs. 8a and 8c are likely where debris is less concentrated, allowing the rain to increase the diversity of scatterers, causing ρ_{hv} to lower.

Last, the metal sheet TDS exhibits a very commonly observed, horizontal TDS structure (Fig. 8e) with a distinct, circular region of low ρ_{hv} near the center of the updraft. The concentration of metal sheets corresponds with the lower values of ρ_{hv} as well (Fig. 8f). For each TDS in Fig. 8, most of the debris are inside of the outermost 10 m s^{-1} updraft contour.

2) TORNADO DISSIPATION CASE

The evolution of ρ_{10} and Z_{90} for a tornado dissipation case are shown in Fig. 9. For all debris types, ρ_{10} increases as the tornado weakens (Figs. 9a,c,e). Weaker vertical velocities lead to less lofted debris, causing higher values of ρ_{10}. Once again, the range in the change in ρ_{10} for the wood boards is much wider than that for the leaf and metal sheet TDS. Near the end of the simulation, the updraft briefly intensifies. In response, ρ_{10} for the metal sheets decreases slightly. The same holds true for the leaves, but the decrease is very small with the wood boards showing little to no decrease in ρ_{10}.

Like in the genesis case, changes in ρ_{10} were also assessed for points only within the TDS (not shown). The trends in ρ_{10} were not significant for all debris types. However, for all debris types, ρ_{10} became more variable following decreases in W_{99} and $V_{H,99}$. Furthermore, ρ_{10} at 17.5° had little to no trend, once again indicating that debris was not lofted near the top of the SimRadar domain.

When the tornado weakens, the TDS area for each debris type generally decreases (Figs. 10a–c). This is contrary to results from Houser et al. (2016), where the lower portions of the TDS widened as the tornado weakened. However, in Houser et al. (2016) debris fallout from the parent storm caused the TDS at lower levels to widen. Due to the shallow LES domain used in this study, the debris was not lofted as high as could be seen in observations, making the fallout signature not appear in these results.

Each TDS area decreases sharply near 500 s, which occurs prior to the weakening of the updraft at 400 s (Fig. 10). The rate of change of each TDS area is 90 m^2 s^{-1} for the leaves, 66 m^2 s^{-1} for the wood boards, and 154 m^2 s^{-1} for the metal sheets. The leaf and metal sheet TDS area decreases at a greater rate than what is seen in the genesis case (26 m^2 s^{-1} for leaves and 94 m^2 s^{-1} for metal sheets). However, the TDS area for the wood boards changes at a similar rate in both the dissipation and genesis simulations. The TDS area defined by the 0.8 ρ_{hv} threshold is also shown in Fig. 10. Using the

Brought to you by NOAA Central Library | Unauthenticated | Downloaded 01/23/24 09:18 PM UTC

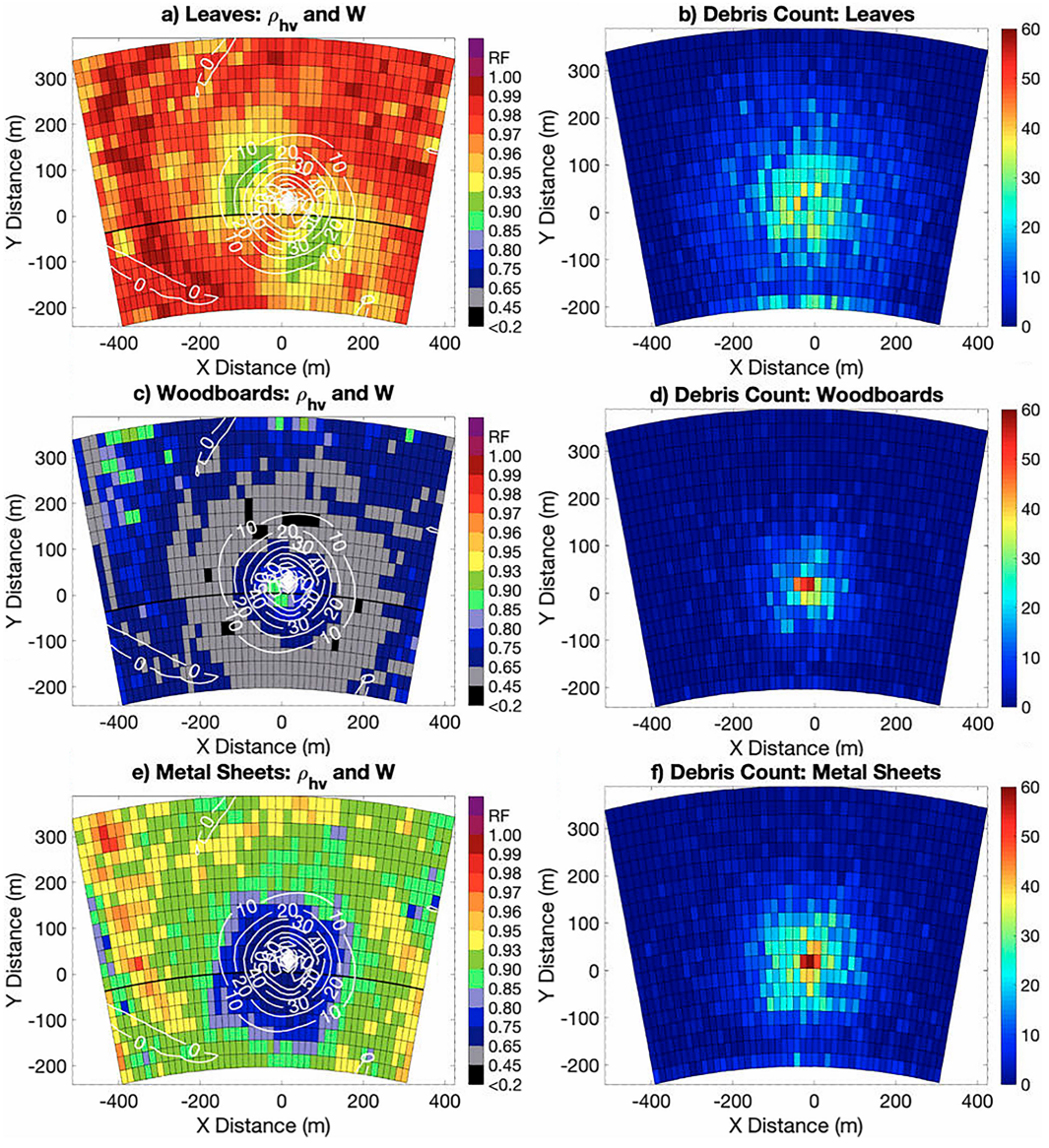

FIG. 8. PPI plots of ρ_{hv} (color fill) and vertical velocity (white contours) for (a) leaves, (c) wood boards, and (e) metal sheets at 2.5° elevation (89 m AGL). Also shown is the debris concentration for (b) leaves, (d) wood boards, and (f) metal sheets for a range-gate resolution of 75 m. The black line across each of the PPIs in (a), (c), and (e) is where the vertical cross section in Fig. 16, described later, is taken.

0.8 ρ_{hv} criteria, the wood board TDS area exhibits a sharper decrease, indicating a faster rate of decrease in the TDS area, while the metal sheet TDS decreases less drastically. Like in the genesis simulation, the leaf TDS is barely detectable using the 0.8 ρ_{hv} threshold (Fig. 10a). Thus, changes in the wood board and metal TDS are sensitive to the selected ρ_{hv} criteria while changes in the leaf TDS are best seen using a higher ρ_{hv} threshold.

c. *Cumulative tornadogenesis simulation*

To emulate a realistic TDS, similar to tornadoes in nature with multiple debris types, cumulative simulations were run with equal amounts of each debris type. The results of these two tornadogenesis simulations are presented in this section.

In comparing PPIs at 2.5° elevation at the end of each simulation (Fig. 11), it is seen that the TDS area widens as debris concentration increases. The TDS with a lower debris concentration (Fig. 11a) is mostly bound by the 10 m s^{-1} updraft contour, whereas the higher-debris-concentration TDS (Fig. 11b) extends beyond the updraft core. By visual observation, the lowest values of ρ_{hv} are very similar in both simulations and are located to the northwest and southeast of the vortex center. The primary difference between the lowest values of ρ_{hv} in these two simulations is the areal extent, with the

Brought to you by NOAA Central Library | Unauthenticated | Downloaded 01/23/24 09:18 PM UTC

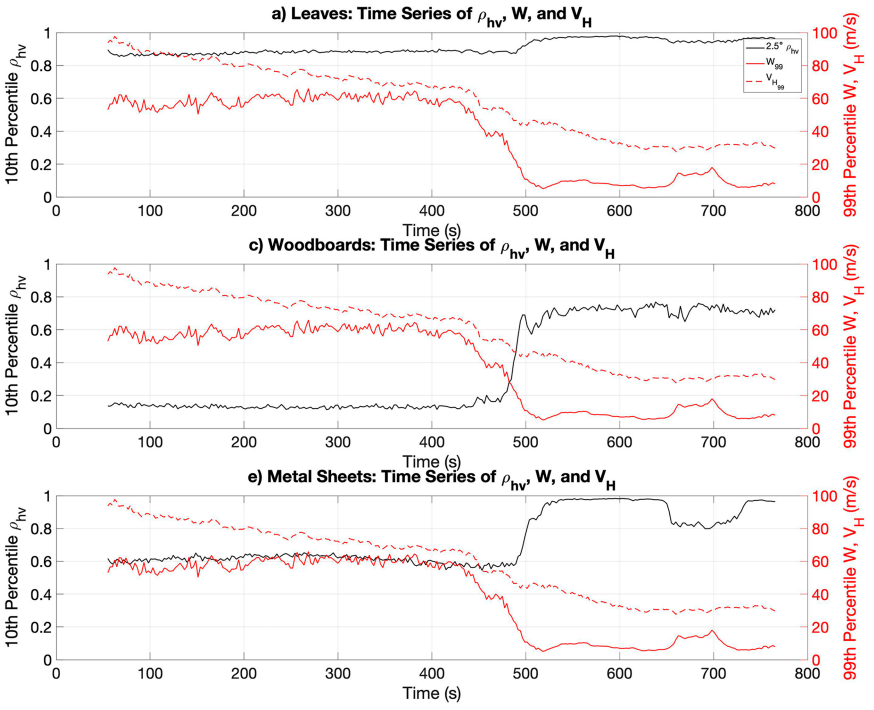

FIG. 9. Time series plots of ρ_{10} for (a) leaves, (b) wood boards, and (c) metal sheets at 2.5° (solid black line). On each graph, W_{99} (red line) and $V_{H,99}$ (red dashed line) are also plotted for values at 89 m. All values shown are from the dissipation simulation.

higher-concentration case having a larger region of $\rho_{hv} < 0.2$. In both cumulative simulation PPIs (Fig. 11), there is a lack of a high ρ_{hv} center as seen in Fig. 8c, suggesting that the high ρ_{hv} was likely caused by a lack of scatterer diversity.

While there is seemingly a visual correlation between the lowest values of ρ_{hv} and the highest vertical wind speeds, there is no trend relating the two parameters (not shown). It is likely that, while low ρ_{hv} often resides near the updraft,

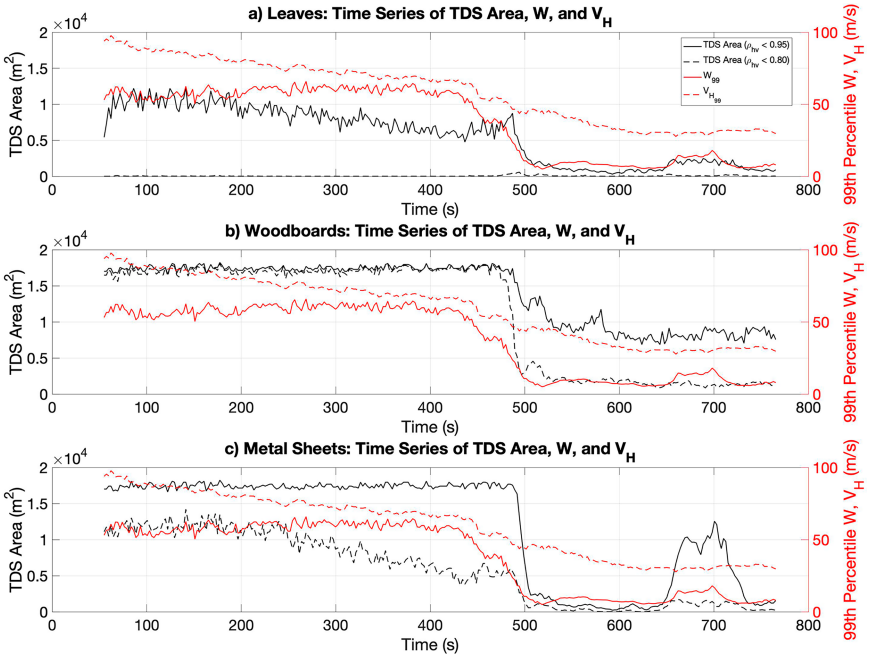

FIG. 10. As in Fig. 7, but for the dissipation simulation.

Brought to you by NOAA Central Library | Unauthenticated | Downloaded 01/23/24 09:18 PM UTC

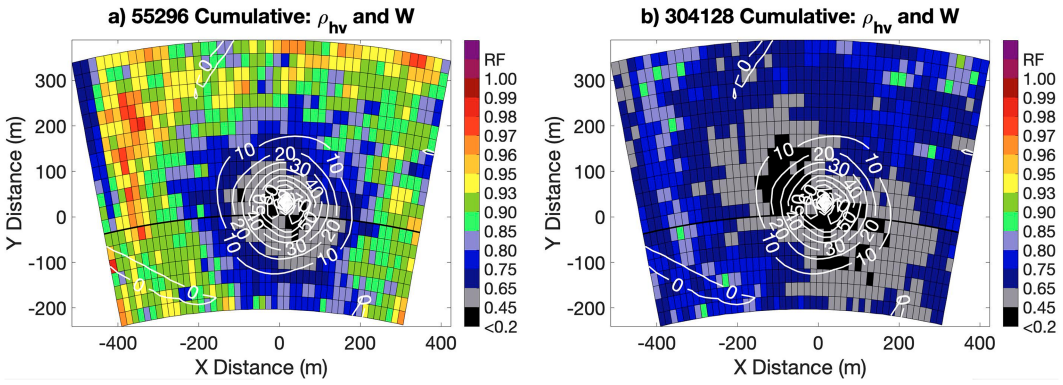

FIG. 11. PPI plots of ρ_{hv} (color fill) and vertical velocity (white contours) at 2.5° (89 m AGL) for the (a) lower-concentration and (b) higher-concentration cumulative simulations.

there is not always a one-to-one, spatial correlation between ρ_{hv} and vertical wind speeds. A factor contributing to the lack of correlation could be the relatively high resolution of the SimRadar grid (75-m range gates). Operational radars have coarser spatial resolution, and at larger spatial scales the correlation between ρ_{hv} and updraft speed could be higher. However, there is a trend in vertical velocity and debris concentration, as seen in Fig. 12. Each debris type exhibits an increasing trend, with debris in lower concentrations clustering at low vertical velocities and becoming more varied at higher velocities. The correlation between concentration and vertical velocity for all debris types is equal to or larger than 0.7, with metal sheets having the highest correlation. It is not surprising that the debris with the lowest mass (leaves) has the lowest correlation. As previously shown, weaker vertical velocities can loft leaves into the tornado but not heavier debris types, such as wood boards or metal sheets. Thus, higher concentrations of leaves can exist at lower updraft speeds while heavier debris types will have a more linear relationship between concentration and vertical velocity.

For the vertical distribution of average values of Z_{90}, Fig. 13 shows higher values of Z_{90} at 2.5° that then decrease with height. This reduction is likely due to debris falling out of the updraft, thus reducing the debris concentration at higher heights. The cumulative simulation with a higher debris concentration experiences the largest change of Z_{90} with height, with the average Z_{90} changing by about 5–6 dB from 50 to 611 m. The metal sheet simulation experiences the least amount of change of Z_{90} with height with the average Z_{90} changing only by 1 dB from 50 to 318 m.

To examine the evolution of ρ_{10} throughout the tornadogenesis simulation, ρ_{10} is plotted across time and height in Fig. 14. In both simulations, the TDS height initially increases

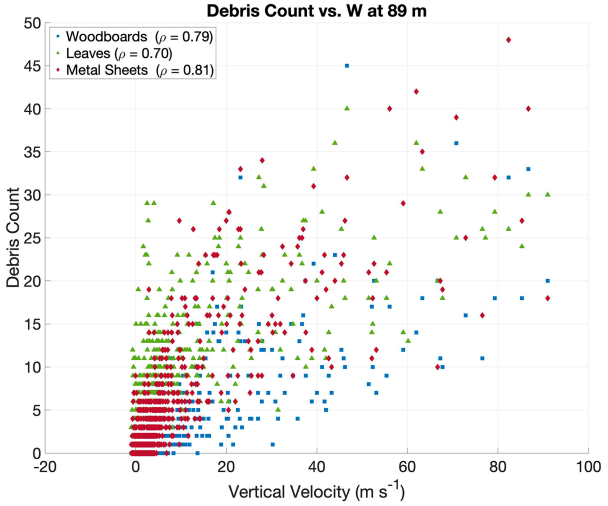

FIG. 12. Debris concentration in each radar gate is plotted against vertical velocity for wood boards (blue), leaves (green), and metal sheets (red) at 89 m AGL. The correlation coefficients between concentration and vertical velocity for each debris type are given in the legend. Values of debris concentration and vertical velocity are valid for the end of the tornadogenesis simulation.

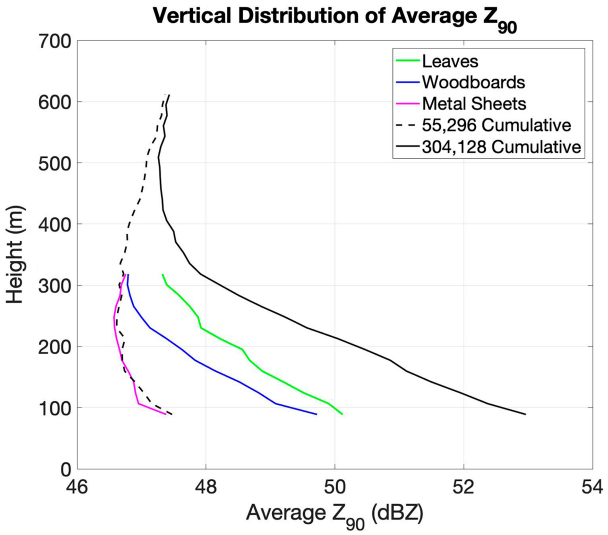

FIG. 13. Vertical profile of average Z_{90} across the last 24 s of the tornadogenesis simulation for each debris type and each cumulative simulation. There are 101 376 debris items in the single-volume simulations.

Brought to you by NOAA Central Library | Unauthenticated | Downloaded 01/23/24 09:18 PM UTC

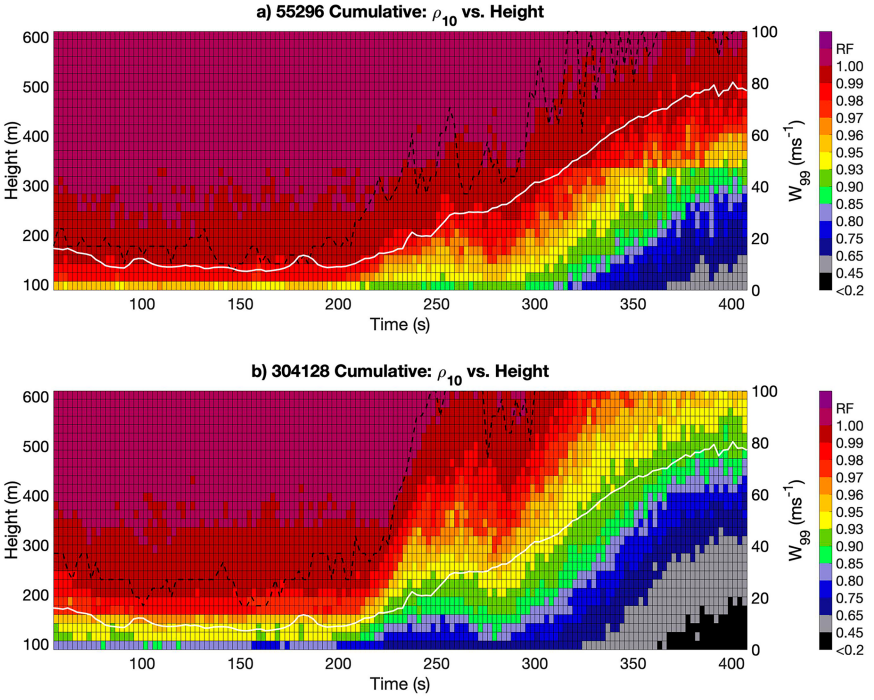

FIG. 14. Time–height plots of ρ_{10} (color fill), W_{99} at 89 m AGL (white line), and TDS height (black dashed line) for the (a) the lower-debris-concentration cumulative simulation and (b) higher-debris-concentration cumulative simulation.

between 200 and 250 s with increasing W_{99} (Fig. 14). However, between 250 and 275 s the TDS height levels off despite an intensifying updraft. To explain the lack of increase in TDS height, the structure of the vortex was examined. At 200 s, there are two, small vortices that rotate around a common origin (not shown). Between 200 and 275 s, the vortices briefly merge before breaking apart. Furthermore, a core of weaker winds descends to the bottom of the domain near 260 s, which is when the TDS height begins to level off.

In both simulations, the maximum peak TDS height is 611 m, which is the maximum height seen by the radar beam. However, despite having the same peak height, $\rho_{10} < 0.2$ reaches a higher elevation in the higher-debris-concentration simulation (Fig. 14b). The rate of change of the TDS height also differs between the two simulations. The TDS height for the lower-concentration simulation goes from 124 to 611 m AGL within 170 s, which is a rate of change of 2.9 m s^{-1}. Meanwhile, the higher-concentration simulation goes from 177 to 611 m AGL within 84 s, which is a rate of change of 5.2 m s^{-1}.

To see the actual distribution of debris, a plot of the location of each piece of debris and histograms of the count of debris were made for the lower-concentration cumulative simulation (Fig. 15). For leaves and metal sheets, 50% of debris exist below 130 m whereas 50% of wood boards reside below 110 m. It is reasonable that more of the lightest debris type (leaves) is lofted relative to heavier debris. However, metal sheets are the heaviest debris, yet at the highest elevations there exist more metal sheets than wood boards or leaves. It is not known why this was the case, but it could be attributed to the shape and aerodynamics of the metal sheet as compared with the other debris types.

The wood boards are concentrated within 60 m to the east and west of the origin, the metal sheets are concentrated within 80 m, and the leaves are mostly contained within 120 m (Fig. 15). This means the largest diversity of concentrated debris exists within 60 m of the origin and below 110 m. On the edges of the domain away from the strong updraft, descending debris dominates, with most of the descending debris being leaves (Fig. 15a). These observations are compared with a cross section of ρ_{hv} through the center of the vortex (Fig. 16). The exact path of the cross sections is represented by the black lines in the PPI plots in Fig. 8. Values of ρ_{hv}, vertical velocity, and horizontal velocity in these cross sections were averaged across the last 24 s of the tornadogenesis simulation.

The lowest values of ρ_{hv} in Fig. 16a are within the region with the highest concentration of diverse scatterers (within 60 m from the origin and below 110 m). These low values of ρ_{hv} are also located near the strongest vertical and horizontal wind speeds. There are fewer debris above 130 m AGL, especially wood boards (Fig. 15b), meaning the top of the $\rho_{hv} < 0.65$ tower is dominated by leaves and metal sheets (Fig. 16a). The reduction of debris with height also relates to the lower Z_H values at higher elevations (Fig. 13). In addition, the width of the $\rho_{hv} < 0.65$ tower in Fig. 16 is mostly within 100 m of the origin, which matches where most of the wood boards and metal sheets reside in Figs. 16b and 16c. Last, past 200 m from the center of the vortex, ρ_{hv} begins to increase

Brought to you by NOAA Central Library | Unauthenticated | Downloaded 01/23/24 09:18 PM UTC

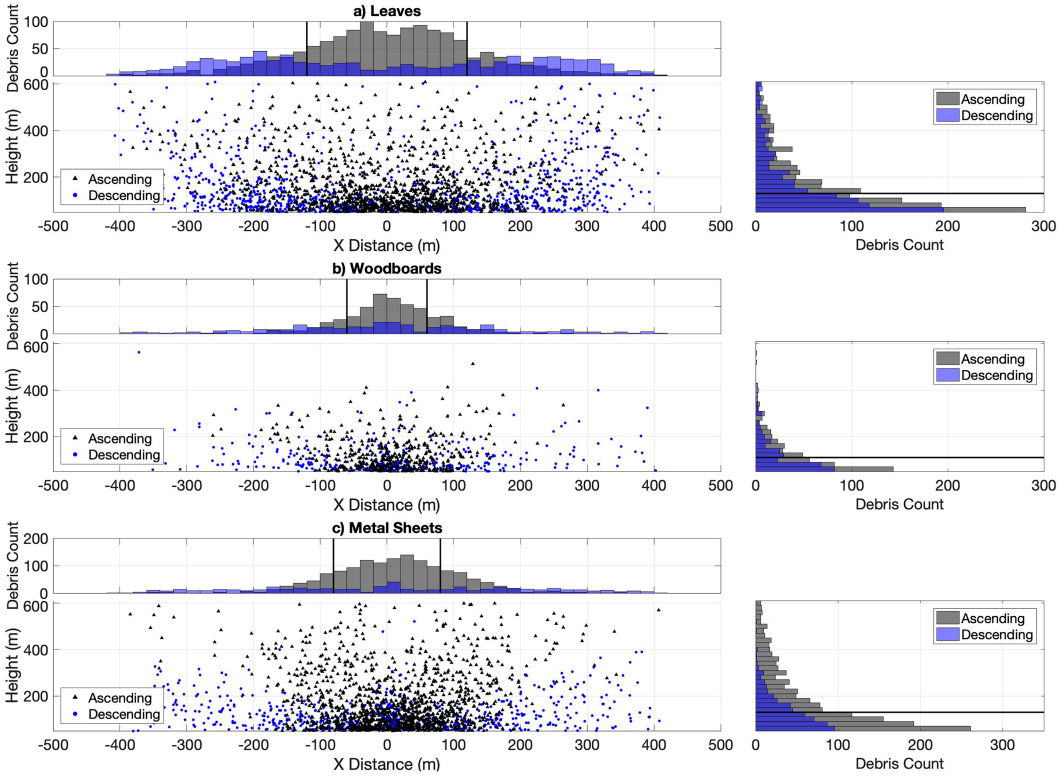

FIG. 15. Vertical view along the x axis of the location of each debris type for the lower-concentration cumulative simulation for (a) leaves, (b) wood boards, and (c) metal sheets. Black dots represent ascending debris, and blue dots represent descending debris. The histograms over the vertical views represent a count of debris along the x axis, and the histograms at the right of the vertical views represent a count of debris along the z axis. Fifty percent of debris exists within and below the black lines in each histogram plot. Only debris within the radar beam were considered such that debris at the bottom of the domain would not bias the measured counts.

(Fig. 16a). Most of the ascending debris are within 200 m from the origin, meaning the higher ρ_{hv} values likely correspond to debris fallout. Concentrations of wood boards and metal sheets are low at these farther distances, with leaves mostly corresponding to the higher ρ_{hv} values seen on the edge of the domain (Fig. 16a).

A comparison of the vertical structure in both simulations shows that they look similar to what is seen in observational cases (e.g., Kurdzo et al. 2015; Wakimoto et al. 2015; Griffin et al. 2017, 2019), with lower ρ_{hv} located near the maximum updraft and some debris fallout to the east and west of the TDS (Fig. 16). The width of the TDS is mostly bound by the 20 m s^{-1} updraft and 50 m s^{-1} horizontal velocity contours for the lower-concentration case (Fig. 16a). Since the TDS is wider for the higher-debris-concentration simulation, the debris is mostly bound by the 10 m s^{-1} updraft and 40 m s^{-1} horizontal velocity contours (Fig. 16b).

4. Discussion

A summary of the specific hypotheses this project examined is presented in Table 6. The first four hypotheses relate to relationships explored using the single-volume emulator while the latter four correspond to those examined using SimRadar. How strongly this study supported a given hypothesis was assessed using both correlation coefficients (see values in leftmost column in Table 6), in addition to a qualitative assessment of the results in section 4. A hypothesis was considered strongly supported if the correlation coefficient for each debris type exceeded ±0.80, conditionally supported if *at least* one debris type exceeded ±0.80, and not supported if all debris types were less than ±0.80. For hypotheses regarding the strength of the vortex, correlation coefficients ρ were calculated with vertical velocity and the parameter in question. Since horizontal and vertical velocities are highly correlated ($\rho = 0.99$) at 89 m, it was assumed that, if a parameter was correlated with vertical velocity, it was also correlated with the horizontal velocity. Each correlation coefficient value was calculated at a height of 89 m AGL (2.5° elevation) to be consistent with the height primarily analyzed in section 4.

Both decreases in ρ_{hv} and increases in Z_H with increasing debris size are conditionally supported by the simulations performed in this study. The relationship between ρ_{hv} and debris size was more apparent for wood boards than it was for rocks since rocks had oscillating values of ρ_{hv} for larger sizes. Values of Z_H increase rapidly for smaller debris. However, for larger debris the increase is more gradual and, in some cases, nearly constant due to resonance effects in the Mie scattering

Brought to you by NOAA Central Library | Unauthenticated | Downloaded 01/23/24 09:18 PM UTC

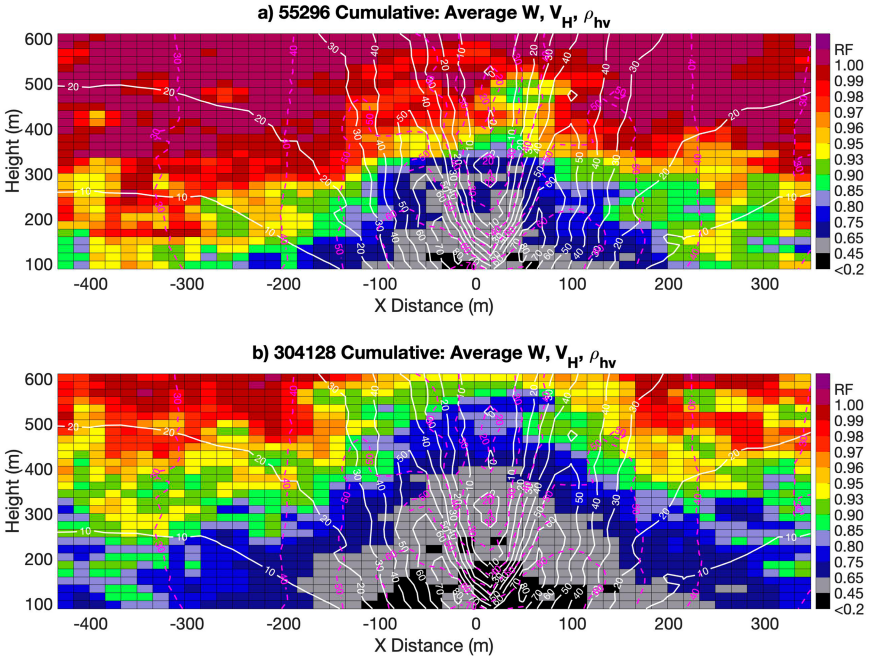

FIG. 16. Vertical cross sections showing averaged values of ρ_{hv} (color fill), vertical velocity (white contours), and horizontal velocity (dashed pink contour) across the last 24 s of the tornadogenesis simulation for the (a) lower-concentration and (b) higher-concentration cumulative simulations. These cross sections are taken along the x axis through the center of the vortex.

regime. In general, the polarimetric variables appear to distinguish classes of debris sizes from one another well. However, quantitative sizing algorithms might be challenging due to nonmonotonic relationships.

While the relationship between ρ_{hv} and increasing debris concentration is not statistically significant, values of ρ_{hv} for both wood boards and rocks did decrease with increasing debris concentration with the introduction of a uniform rain background. The decrease in ρ_{hv} depends on the ratio of debris to rain, with decreases in ρ_{hv} becoming more prominent when one scatterer type was not completely dominating the signal. Meanwhile, Z_H does depend on debris concentration since Z_H is related to the number concentration of scatterers.

Values of ρ_{10} decrease during tornado intensification for each debris type. As one of the most strongly supported hypotheses in this study, it confirms that decreases of ρ_{hv} within the TDS are an indication of an intensifying vortex, regardless of the lofted debris types. Values of ρ_{10} for leaves are consistently higher than 0.80, which is the ρ_{hv} threshold for TDSs proposed by Ryzhkov et al. (2005b), while wood boards and metal sheets can have ρ_{hv} values lower than 0.75. The results of this study show that, since different debris types have varying ranges of ρ_{10}, an intense tornado can have values of ρ_{10} greater than 0.80 depending on the debris type.

The ranges of ρ_{10} for each debris type, as seen by an S-band radar during tornadogenesis, are given in Fig. 17. When the vortex intensifies, ρ_{10} for the leaf TDS varies between 0.95 and 0.99, the wood board TDS between 0.1 and 0.8, and the metal sheet TDS between 0.6 and 0.99. The range of ρ_{10} for different debris types provides a caveat to the operational applications of the TDS to infer information about tornado intensity or damage severity. Wakimoto et al. (2018, 2020) found that tornado intensity correlates with a drop in correlation coefficient during the intensification stage of two different tornadoes. However, given the consistently high values of ρ_{10} for the leaves in this study, an intense tornado could have high values of ρ_{hv} if only small debris are available to be lofted. *With this in mind, it is the change in minimum* ρ_{hv} *over time that can serve as an indication of tornadic intensity*. Furthermore, in the presence of similar debris types, the lofting of larger or more debris can reduce ρ_{hv}. In the case of the latter, the required concentration of lofted debris needed to lower ρ_{hv} depends on the signal power (and thus the size, if in the Rayleigh scattering regime) of rain. If debris dominates the signal, then ρ_{hv} will decrease; however, the magnitude of this decrease is less for smaller debris types.

These findings do not dismiss the potential for quantitative thresholds of TDS characteristics to predict tornadic intensity (e.g., ρ_{hv} of abc implies EFx), but rather, they highlight an important caveat that debris availability impacts the TDS. Furthermore, the traditional criteria used to define a TDS does not always apply in select cases when similar debris types are lofted. However, under normal circumstances when a tornado lofts a variety of debris types, these caveats are not a concern. Thus, the degree to which ρ_{hv} decreases in the TDS could further be an indicator of what types of debris, and thus damage, are occurring in addition to potential quantitative thresholds.

Brought to you by NOAA Central Library | Unauthenticated | Downloaded 01/23/24 09:18 PM UTC

TABLE 6. List of hypotheses tested in this study along with the corresponding correlation coefficients for each applicable debris type. Hypotheses are considered to be strongly supported if all of the debris has $\rho > 0.8$, conditionally supported if only some debris types have $\rho > 0.8$, and not supported if all debris types have $\rho < 0.8$. An asterisk signifies results where there are caveats to the results in addition to the values of ρ.

TDS hypotheses	Findings	Correlation coef
As debris size increases, ρ_{hv} will decrease	Conditionally supported	Rock: −0.72 Wood board: −0.84
As debris size increases, Z_H will increase	Conditionally supported	Rock: 0.71 Wood board: 0.90
As debris concentration increases, ρ_{hv} will decrease	Not supported*	Rock: −0.43 Rock + rain: −0.49 Wood board: 0.20 Wood board + rain: −0.57
As debris concentration increases, Z_H will increase	Strongly supported	Rock: 0.82 Rock + rain: 0.87 Wood board: 0.82 Wood board + rain: 0.91
As a tornado intensifies, ρ_{hv} will decrease	Strongly supported	Leaf: −0.98 Wood board: −0.87 Metal sheet: −0.98
As a tornado intensifies, Z_H will increase	Conditionally supported	Leaf: 0.81 Wood board: 0.44 Metal sheet: 0.41
As a tornado intensifies, the TDS area will increase	Strongly supported	Leaf: 0.87 Wood board: 0.89 Metal sheet: 0.96
As a tornado intensifies, the TDS height will increase	Conditionally supported	Leaf: 0.91 Wood board: 0.95 Metal sheet: 0.77

The spatial TDS parameters (TDS area and height) were also good indicators of an intensifying tornado. Increases in the TDS area exhibited a strong correlation with a strengthening updraft. Since the vertical and horizontal velocities increased in tandem with one another, this implies increases to TDS area are also correlated strongly with intensifying horizontal wind speeds. TDS height was also numerically assessed in this study. Increases in TDS height are well correlated with increases in the updraft speed for most debris types (Table 6). However, while TDS height generally increases with an intensifying updraft, debris ejection and/or fallout can make this relationship nonlinear.

Similar temporal behavior of TDS structure is seen in observations and simulations. For each debris type, ρ_{10} decreased at higher altitudes over time, similar to Griffin et al. (2019). Griffin et al. (2019) hypothesized that the TDS took time to become homogeneous with height since heavier debris pieces take longer to reach higher elevations. In the simulations, a similar temporal pattern is seen with large vertical gradients in ρ_{hv} when wood boards are concentrated near the surface during early periods, followed by a more homogeneous vertical profile of low ρ_{hv} at later stages with strong updrafts and debris mixed throughout.

5. Conclusions

Past research has resulted in numerous hypotheses regarding relationships among the TDS, polarimetric radar variables, and the three-dimensional, tornadic wind field. Unlike observational data, the simulations conducted herein provide the ability to relate debris size, type, and concentration to both polarimetric radar data and the dynamic wind field, allowing for the deeper exploration of these observational hypotheses. To do this, two radar emulators were used: a single-volume emulator and a more complex, dual-polarization radar simulator called SimRadar. Scattering amplitudes for

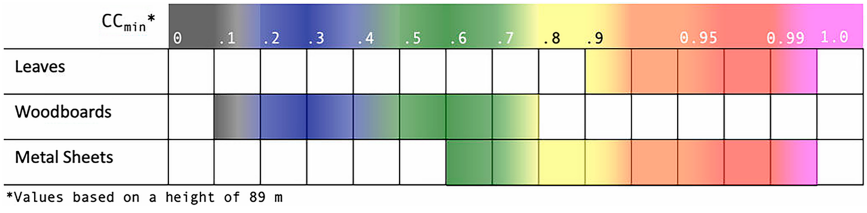

FIG. 17. Range of values for ρ_{10} for each debris type used in the SimRadar simulations. These values were taken from the individual tornadogenesis simulations at a height of 89 m.

Brought to you by NOAA Central Library | Unauthenticated | Downloaded 01/23/24 09:18 PM UTC

debris were obtained using two methods. The first method was T-matrix calculations that allowed for a larger distribution of debris sizes, while the second method used HFSS calculations that provide more accurate scattering calculations for each debris type.

For rocks and wood boards, ρ_{hv} is generally lower and Z_H higher for larger pieces of debris. Likewise, ρ_{hv} decreases and Z_H increases when more debris is present amid other hydrometeors. Another factor that impacts ρ_{hv} is the dielectric constant, meaning different debris types can produce drastically different ρ_{hv} values for a given debris size.

Looking at trends within in TDS over time, the SimRadar simulations revealed that values of ρ_{hv} decrease and TDS height and area increase as a tornado intensifies. These findings support the observational hypotheses that spatial and statistical parameters of the TDS can be used to qualitatively identify changes in tornado intensity. However, since smaller and less reflective debris types typically have relatively high values of ρ_{hv}, a strong tornado could have a TDS that is less evident in ρ_{hv} if limited debris are available. Furthermore, these trends were most apparent at lower elevation angles. Operational radars, which typically scan at higher elevation angles than SimRadar, might not always observe these trends of ρ_{hv} within the TDS.

Both cumulative simulations produced the most realistic looking TDSs with low ρ_{hv} near the updraft core. Larger concentrations of debris produced a wider TDS, though the lowest values of ρ_{hv} were similar across both cumulative simulations. Values of average Z_H decreased with height in all simulations, although the largest decrease occurred in the cumulative simulation with the higher debris concentration. In the lower-debris-concentration cumulative simulation, the lowest ρ_{hv} values were associated with the largest diversity of scatterers. There was also vertical stratification of debris, with wood boards confined to the lowest 110 m and mostly leaves and metal sheets reaching the top of the domain. Higher values of ρ_{hv} outside the updraft core were associated with lower concentrations of debris that were falling out on the periphery of the vortex.

One limitation of this study is a lack of a full-scale, parent thunderstorm in the simulations. Seeing how other dynamical properties can affect the evolution of the TDS could also prove beneficial. In select cases, storm-scale winds have advected debris away from the parent vortex and can thus play a role in the structure of the TDS. Looking at the influence of storm-scale winds from a simulation and an observational framework could provide a more detailed analysis of the TDS than what was performed in this study. Additionally, other debris types could be explored, such as bricks or insulation.

Also, while the high azimuthal resolution in SimRadar is useful for examining the fine-scale detail within the TDS, an operational radar will not be able to resolve such detail since the observation distance will be greater. However, these higher resolution simulations show the same general trends in TDS area, ρ_{hv}, and so on, that have been documented in observational studies with operational radars and higher-resolution mobile systems.

While this work focused primarily on simulations, it would also be beneficial to add an observational component to this work. Since there are distinctive differences between the values of ρ_{hv} and the structure of TDSs composed of different debris, it would be interesting to simulate debris for an observed tornado based on damage surveys. Although the exact number of debris in real cases is unknown, the types of debris lofted and tornadic wind speeds can be modeled to better represent what is seen in observed radar data. The spatial and statistical features of the simulated TDS can then be compared with the observed data for further analysis. Simulating other wavelengths, especially those used by mobile radars, could also prove useful. Further examining these relationships between polarimetric characteristics of the TDS and specific debris types and sizes could yield more specific information to researchers and operational forecasters to improve interpretation of TDSs and mitigate debris centrifuging bias.

Acknowledgments. We want to thank Dr. Phillip Chilson for his feedback as well as Professor Takanori Uchida at Kyushu University for providing the RIAM-COMPACT software and allowing its use for this research project. We would also like to thank Dr. Jana Houser and two other anonymous reviewers for their invaluable feedback. This project was supported by the National Science Foundation (NSF) under Grants AGS-1823478 and AGS-2114817.

Data availability statement. Those interested in using the code and data from this project can contact the corresponding author. The source code for SimRadar is widely accessible through GitHub (https://github.com/OURadar/SimRadar).

REFERENCES

Balakrishnan, N., and D. S. Zrnić, 1990: Use of polarization to characterize precipitation and discriminate large hail. *J. Atmos. Sci.*, **47**, 1525–1540, https://doi.org/10.1175/1520-0469(1990)047<1525:UOPTCP>2.0.CO;2.

Bluestein, H. B., M. M. French, R. L. Tanamachi, S. Frasier, K. Hardwick, F. Junyent, and A. Pazmany, 2007: Close-range observations of tornadoes in supercells made with a dual-polarization, X-band, mobile Doppler radar. *Mon. Wea. Rev.*, **135**, 1522–1543, https://doi.org/10.1175/MWR3349.1.

Bodine, D. J., M. R. Kumjian, R. D. Palmer, P. L. Heinselman, and A. V. Ryzhkov, 2013: Tornado damage estimation using polarimetric radar. *Wea. Forecasting*, **28**, 139–158, https://doi.org/10.1175/WAF-D-11-00158.1.

——, R. D. Palmer, and G. Zhang, 2014: Dual-wavelength polarimetric radar analyses of tornadic debris signatures. *J. Appl. Meteor. Climatol.*, **53**, 242–261, https://doi.org/10.1175/JAMC-D-13-0189.1.

——, T. Maruyama, R. D. Palmer, C. J. Fulton, H. B. Bluestein, and D. C. Lewellen, 2016a: Sensitivity of tornado dynamics to debris loading. *J. Atmos. Sci.*, **73**, 2783–2801, https://doi.org/10.1175/JAS-D-15-0188.1.

——, R. D. Palmer, T. Maruyama, C. J. Fulton, Y. Zhu, and B. L. Cheong, 2016b: Simulated frequency dependence of radar observations of tornadoes. *J. Atmos. Oceanic Technol.*, **33**, 1825–1842, https://doi.org/10.1175/JTECH-D-15-0120.1.

Bukovčić, P., D. Zrnić, and G. Zhang, 2017: Winter precipitation liquid–ice phase transitions revealed with polarimetric radar

Brought to you by NOAA Central Library | Unauthenticated | Downloaded 01/23/24 09:18 PM UTC

and 2DVD observations in central Oklahoma. *J. Appl. Meteor. Climatol.*, **56**, 1345–1363, https://doi.org/10.1175/JAMC-D-16-0239.1.

Cheong, B. L., D. J. Bodine, C. J. Fulton, S. M. Torres, T. Maruyama, and R. D. Palmer, 2017: SimRadar: A polarimetric radar time-series simulator for tornadic debris studies. *IEEE Trans. Geosci. Remote Sens.*, **55**, 2858–2870, https://doi.org/10.1109/TGRS.2017.2655363.

Church, C. R., J. T. Snow, G. L. Baker, and E. M. Agee, 1979: Characteristics of tornado-like vortices as a function of swirl ratio: A laboratory investigation. *J. Atmos. Sci.*, **36**, 1755–1776, https://doi.org/10.1175/1520-0469(1979)036<1755:COTLVA>2.0.CO;2.

Cross, R. N., 2021: Exploring tornado debris signature hypotheses using radar simulations and large-eddy simulations. M.S. thesis, School of Meteorology, University of Oklahoma, 118 pp.

Dowell, D. C., C. R. Alexander, J. M. Wurman, and L. J. Wicker, 2005: Centrifuging of hydrometeors and debris in tornadoes: Radar-reflectivity patterns and wind-measurement errors. *Mon. Wea. Rev.*, **133**, 1501–1524, https://doi.org/10.1175/MWR2934.1.

French, M. M., H. B. Bluestein, I. PopStefanija, C. A. Baldi, and R. T. Bluth, 2014: Mobile, phased-array, Doppler radar observations of tornadoes at X band. *Mon. Wea. Rev.*, **142**, 1010–1036, https://doi.org/10.1175/MWR-D-13-00101.1.

Gibbs, J. G., 2016: A skill assessment of techniques for real-time diagnosis and short-term prediction of tornado intensity using the WSR-88D. *J. Oper. Meteor.*, **4**, 170–181, https://doi.org/10.15191/nwajom.2016.0413.

Griffin, C. B., D. J. Bodine, and R. D. Palmer, 2017: Kinematic and polarimetric radar observations of the 10 May 2010, Moore–Choctaw, Oklahoma, tornadic debris signature. *Mon. Wea. Rev.*, **145**, 2723–2741, https://doi.org/10.1175/MWR-D-16-0344.1.

——, ——, J. M. Kurdzo, A. Mahre, and R. D. Palmer, 2019: High-temporal resolution observations of the 27 May 2015 Canadian, Texas, tornado using the Atmospheric Imaging Radar. *Mon. Wea. Rev.*, **147**, 873–891, https://doi.org/10.1175/MWR-D-18-0297.1.

Houser, J. L., H. B. Bluestein, and J. C. Snyder, 2015: Rapid-scan, polarimetric, Doppler radar observations of tornadogenesis and tornado dissipation in a tornadic supercell: The "El Reno, Oklahoma" storm of 24 May 2011. *Mon. Wea. Rev.*, **143**, 2685–2710, https://doi.org/10.1175/MWR-D-14-00253.1.

——, ——, and ——, 2016: A fine-scale radar examination of the tornadic debris signature and weak-echo reflectivity band associated with a large, violent tornado. *Mon. Wea. Rev.*, **144**, 4101–4130, https://doi.org/10.1175/MWR-D-15-0408.1.

Kosiba, K. A., and J. Wurman, 2013: The three-dimensional structure and evolution of a tornado boundary layer. *Wea. Forecasting*, **28**, 1552–1561, https://doi.org/10.1175/WAF-D-13-00070.1.

Kumjian, M. R., and A. V. Ryzhkov, 2008: Polarimetric signatures in supercell thunderstorms. *J. Appl. Meteor. Climatol.*, **47**, 1940–1961, https://doi.org/10.1175/2007JAMC1874.1.

——, A. P. Khain, N. Benmoshe, E. Ilotoviz, A. V. Ryzhkov, and V. T. J. Phillips, 2014: The anatomy and physics of Z_{DR} columns: Investigating a polarimetric radar signature with a spectral bin microphysical model. *J. Appl. Meteor. Climatol.*, **53**, 1820–1843, https://doi.org/10.1175/JAMC-D-13-0354.1.

Kurdzo, J. M., D. J. Bodine, B. L. Cheong, and R. D. Palmer, 2015: High-temporal resolution polarimetric X-band Doppler radar observations of the 20 May 2013 Moore, Oklahoma, tornado. *Mon. Wea. Rev.*, **143**, 2711–2735, https://doi.org/10.1175/MWR-D-14-00357.1.

Lujan, J., 2016: Radar cross section analysis of tornadic debris. M.S. thesis, School of Electrical and Computer Engineering, University of Oklahoma, 140 pp.

Maruyama, T., 2011: Simulation of flying debris using a numerically generated tornado-like vortex. *J. Wind Eng. Ind. Aerodyn.*, **99**, 249–256, https://doi.org/10.1016/j.jweia.2011.01.016.

McKeown, K., M. M. French, K. S. Tuftedal, H. B. Bluestein, D. W. Reif, and Z. B. Wienhoff, 2020: Rapid-scan and polarimetric radar observations of the dissipation of a violent tornado on 9 May 2016 near Sulphur, Oklahoma. *Mon. Wea. Rev.*, **148**, 3951–3971, https://doi.org/10.1175/MWR-D-20-0033.1.

Mishchenko, M. I., 2000: Calculation of the amplitude matrix for a nonspherical particle in a fixed orientation. *Appl. Opt.*, **39**, 1026–1031, https://doi.org/10.1364/AO.39.001026.

——, L. D. Travis, and D. W. Mackowski, 1996: T-matrix computations of light scattering by nonspherical particles: A review. *J. Quant. Spectrosc. Radiat. Transfer*, **55**, 535–575, https://doi.org/10.1016/0022-4073(96)00002-7.

Ryzhkov, A. V., T. J. Schuur, D. W. Burgess, P. L. Heinselman, S. E. Giangrande, and D. S. Zrnić, 2005a: The Joint Polarization Experiment: Polarimetric rainfall measurements and hydrometeor classification. *Bull. Amer. Meteor. Soc.*, **86**, 809–824, https://doi.org/10.1175/BAMS-86-6-809.

——, ——, ——, and D. S. Zrnić, 2005b: Polarimetric tornado detection. *J. Appl. Meteor.*, **44**, 557–570, https://doi.org/10.1175/JAM2235.1.

Schultz, C. J., and Coauthors, 2012: Dual-polarization tornadic debris signatures Part I: Examples and utility in an operational setting. *Electron. J. Oper. Meteor.*, **13** (9), 120–137, http://nwafiles.nwas.org/ej/pdf/2012-EJ9.pdf.

Senior, T. B., K. Sarabandi, and F. T. Ulaby, 1987: Measuring and modeling the backscattering cross section of a leaf. *Radio Sci.*, **22**, 1109–1116, https://doi.org/10.1029/RS022i006p01109.

Snyder, J. C., H. B. Bluestein, V. Venkatesh, and S. J. Frasier, 2013: Observations of polarimetric signatures in supercells by an X-band mobile Doppler radar. *Mon. Wea. Rev.*, **141**, 3–29, https://doi.org/10.1175/MWR-D-12-00068.1.

Straka, J. M., D. S. Zrnić, and A. V. Ryzhkov, 2000: Bulk hydrometeor classification and quantification using polarimetric radar data: Synthesis of relations. *J. Appl. Meteor.*, **39**, 1341–1372, https://doi.org/10.1175/1520-0450(2000)039<1341:BHCAQU>2.0.CO;2.

Tanamachi, R. L., H. B. Bluestein, J. B. Houser, S. J. Frasier, and K. M. Hardwick, 2012: Mobile X-band, polarimetric Doppler radar observations of the 4 May 2007 Greensburg, Kansas, tornadic supercell. *Mon. Wea. Rev.*, **140**, 2103–2125, https://doi.org/10.1175/MWR-D-11-00142.1.

Thurai, M., and V. N. Bringi, 2005: Drop axis ratios from a 2D video disdrometer. *J. Atmos. Oceanic Technol.*, **22**, 966–978, https://doi.org/10.1175/JTECH1767.1.

Ulaby, F. T., T. Bengal, J. East, M. C. Dobson, J. Garvin, and D. Evans, 1988: Measured data. Microwave dielectric spectrum of rocks, University of Michigan Dept. of Electrical Engineering and Computer Science Rep., 33.

Umeyama, A., B. L. Cheong, S. Torres, and D. Bodine, 2018: Orientation analysis of simulated tornadic debris. *J. Atmos. Oceanic Technol.*, **35**, 993–1010, https://doi.org/10.1175/JTECH-D-17-0140.1.

Van Den Broeke, M. S., 2015: Polarimetric tornadic debris signature variability and debris fallout signatures. *J. Appl. Meteor. Climatol.*, **54**, 2389–2405, https://doi.org/10.1175/JAMC-D-15-0077.1.

Brought to you by NOAA Central Library | Unauthenticated | Downloaded 01/23/24 09:18 PM UTC

——, 2017: Polarimetric radar metrics related to tornado life cycles and intensity in supercell storms. *Mon. Wea. Rev.*, **145**, 3671–3686, https://doi.org/10.1175/MWR-D-16-0453.1.

——, and S. T. Jauernic, 2014: Spatial and temporal characteristics of polarimetric tornadic debris signatures. *J. Appl. Meteor. Climatol.*, **53**, 2217–2231, https://doi.org/10.1175/JAMC-D-14-0094.1.

Wakimoto, R. M., N. T. Atkins, K. M. Butler, H. B. Bluestein, K. Thiem, J. Snyder, and J. Houser, 2015: Photogrammetric analysis of the 2013 El Reno tornado combined with mobile X-band polarimetric radar data. *Mon. Wea. Rev.*, **143**, 2657–2683, https://doi.org/10.1175/MWR-D-15-0034.1.

——, Z. Wienhoff, H. B. Bluestein, and D. Reif, 2018: The Dodge City tornadoes on 24 May 2016: Damage survey, photogrammetric analysis combined with mobile polarimetric radar data. *Mon. Wea. Rev.*, **146**, 3735–3771, https://doi.org/10.1175/MWR-D-18-0125.1.

——, ——, ——, D. J. Bodine, and J. M. Kurdzo, 2020: Mobile radar observations of the evolving debris field compared with a damage survey of the Shawnee, Oklahoma, tornado of 19 May 2013. *Mon. Wea. Rev.*, **148**, 1779–1803, https://doi.org/10.1175/MWR-D-19-0215.1.

Wurman, J., and S. Gill, 2000: Fine-scale radar observations of the Dimmitt, Texas (2 June 1995), tornado. *Mon. Wea. Rev.*, **128**, 2135–2164, https://doi.org/10.1175/1520-0493(2000)128<2135:FROOTD>2.0.CO;2.

——, K. Kosiba, and P. Robinson, 2013: In situ, Doppler radar, and video observations of the interior structure of a tornado and the wind–damage relationship. *Bull. Amer. Meteor. Soc.*, **94**, 835–846, https://doi.org/10.1175/BAMS-D-12-00114.1.

——, ——, T. White, and P. Robinson, 2021: Supercell tornadoes are much stronger and wider than damage-based ratings indicate. *Proc. Natl. Acad. Sci. USA*, **118**, e2021535118, https://doi.org/10.1073/pnas.2021535118.

Zrnić, D. S., and A. V. Ryzhkov, 1999: Polarimetry for weather surveillance radars. *Bull. Amer. Meteor. Soc.*, **80**, 389–406, https://doi.org/10.1175/1520-0477(1999)080<0389:PFWSR>2.0.CO;2.

Brought to you by NOAA Central Library | Unauthenticated | Downloaded 01/23/24 09:18 PM UTC